Rockwall permafrost dynamics evidenced by Repeated and Automated Electrical Resistivity Tomography at Aiguille du Midi (3842 m a.s.l., French Alps)

Feras Abdulsamad[1], Josué Bock[1], Florence Magnin[1], Emmanuel Malet[1], André Revil[1], Matan Ben-Asher[1], Jessy Richard[1, 2], Pierre-Allain Duvillard[2], Marios Karaoulis[3], Thomas Condom[4], Ludovic Ravanel[1] and Philip Deline[1]

1. EDYTEM, CNRS - Université Savoie Mont-Blanc, 73370 Le Bourget du Lac, France
2. Naga Geophysics, 229 rue Joseph Fontanet 73000 Chambéry, France
3. School of Geology, Geophysics Department, Aristotle University of Thessaloniki, Thessaloniki, Greece
4. Univ. Grenoble Alpes, IRD, CNRS, INRAE, Grenoble-INP, IGE, 38000 Grenoble, France

Corresponding author: Abdulsamad Feras (feras.abdul-samad@univ-smb.fr)

Emails: feras.abdul-samad@univ-smb.fr; andre.revil@univ-smb.fr; ludovic.ravanel@univ-smb.fr; florence.magnin@univ-smb.fr; mkaraoulis@geo.auth.gr; matan.ben-asher@univ-smb.fr; pierre-allain.duvillard@naga-geophysics.com; josue.bock@laposte.net; emmanuel.malet@univ-savoie.fr; jessy.richard@naga-geophysics.com; thomas.condom@ird.fr; philip.deline@univ-smb.fr

Keywords: Rockwall permafrost dynamics; Active layer thickness; Electrical resistivity tomography; Temperature measurements.

Intended for publication in The Cryosphere

Abstract. Permafrost degradation significantly affects the stability of rockwalls in high altitude regions. Monitoring rockwall permafrost is essential for assessing potential geohazards. Borehole temperature measurements often lack of sufficient spatial representation in such highly heterogeneous ground conditions. Conversely, geoelectrical measurements can provide more comprehensive insights into these dynamics. This study investigates the permafrost dynamics and hydrogeological system at Aiguille du Midi (3842 m a.s.l., French Alps) using repeated and Automated-Electrical Resistivity Tomography (A-ERT) approaches, covering a period of nearly four years (06/2020-12/2023). A total of three geophysical profiles have been installed on three faces of the Aiguille du Midi (N-W, S and E). An autonomous acquisition system for permanent resistivity monitoring and remote data acquisition is implemented. A time-lapse inversion technique is employed to get the temporal and spatial variations of the electrical resistivity at seasonal and interannual time scales. ERT revealed significant variations in active layer thickness across different rock faces, along with a slight decrease in electrical resistivity at depth, indicating permafrost warming over time. The ERT results did not provide clear evidence of water infiltration or accumulation. Using a petrophysical model, calibrated with laboratory measurements of the temperature dependence of electrical resistivity, we estimated the temperature within the frozen zone from the resistivity measurements (under favorable condition at surface). Validation against direct temperature measurements in a 10-m depth borehole along the NW profile, demonstrates an accuracy of approximately ±1 °C. This research underscores the efficacy of ERT as a promising, non-invasive tool for monitoring permafrost dynamics in Alpine environments. It also reveals challenges associated with conducting A-ERT in high mountain environment, where the contact resistance is very high (~500 kΩ) and sometimes intermittent due to factors such as thunder strikes and rockfalls.

1. Introduction

Climate change accelerates the degradation of the permafrost in high-mountains areas worldwide (Smith et al., 2022). In the European Alps, permafrost has warmed up to > 1°C at 10 m depth, especially in bedrock permafrost (Etzelmüller et al., 2020; Magnin et al., 2024; Noetzli et al., 2024). Over the last decade, there has been a continuous increase in rockfall events, particularly those impacting permafrost in the European Alps (Cathala et al., 2024; Jacquemart et al., 2024; Ravanel et al., 2017). Infrastructures located in high altitude are increasingly affected by these events (Duvillard et al., 2021, 2018; Hartmeyer et al. 2020). Permafrost degradation/warming of the rock mass can also locally be accelerated by heat advection through water infiltration in fractures, causing erosion of the ice-infill (Hauck and Hilbich, 2024; Hartmeyer et al. 2020). As a result, a loss of bonding between rock and ice may occur, which in turn alters the mechanical properties of such assemblage (Mamot et al., 2018; Krautblatter et al., 2013). Therefore, understanding the thermo-hydrogeological dynamics of steep Alpine rock faces is essential for assessing potential geohazards associated with permafrost degradation.

To assess permafrost warming, one approach is to directly determine and monitor rockwall temperatures using temperature sensors installed at the rock surface or in boreholes (*e.g.*, Magnin et al., 2024). Although borehole temperature monitoring is still the only direct method to detect the occurrence of permafrost, it provides only point-scale information, while its distribution and evolution can be highly variable in extreme topographical conditions. In addition, boreholes in rockwall at high altitude are logistically difficult to realize. They are also expensive and invasive.

On the other side, geophysical measurements provide higher spatial coverage with respect to boreholes. Various non- or minimally intrusive methods have been applied to evaluate permafrost, including Refraction Seismic Tomography (RST) (*e.g.*, Steiner et al.,

2019; Draebing 2016), Ground Penetrating Radar (GPR) (Campbell et al., 2018), Electrical Resistivity Tomography (ERT) (*e.g.*, Mollaret et al., 2020; Krautblatter and Hauck 2007) and Induced Polarization (IP) (Maierhofer et al., 2024; Abdulsamad et al., 2019; Duvillard et al., 2018; Doetsch et al., 2015). Combined geophysical methods can take advantage of the complementary petrophysical and spatial sensitivities of these different methods. For instance, ERT measurement was combined with RST to evaluate ice, air, water, and rock contents (Mewes et al., 2017; Hauck et al., 2011). Recently, joint inversion of ERT and RST could reduce the uncertainties in the evaluation of air, water, ice and rock contents (Pavoni et al., 2023; Steiner et al., 2021; Mollaret et al., 2020; Wagner et al., 2019). IP measurements (providing tomograms of the electrical conductivity and normalized chargeability) have been recently used to assess the distribution of permafrost temperature, relying on laboratory calibration and a petrophysical (physics-based) model connecting resistivity and normalized chargeability with temperature under frozen and unfrozen conditions (see Moser et al., 2025; Duvillard et al., 2021, 2018, and references therein).

In the last two decades, ERT has become an increasingly popular tool in permafrost studies (*e.g.*, Herring et al., 2023; Farzamain et al., 2020; Magnin et al., 2015a; Krautblatter et al., 2010). Herring et al. (2023) provide a review of the use of ERT method in permafrost research, detailing both the advantages and limitations of this method in such a context. A significant advantage of using electrical resistivity measurements to assess mountain permafrost is that the freezing and thawing of water filling pores are associated with considerable changes in resistivity (generally between one to three orders of magnitude, see Coperey et al., 2019). Because of this sensitivity, electrical resistivity tomograms can be used to assess of the presence and distribution of permafrost.

Repeated ERT measurements at specific time intervals using the same survey geometry can be used to track the temporal and spatial evolution of permafrost over time (*e.g.*, Offer et

al., 2025, Hilbich et al., 2008). However, rapid changes due to water flow, infiltration or drainage (such as during snowmelt or rainfall) may not be captured by monthly or seasonally repeated measurements (Krautblatter et al., 2010). Alternatively, continuous resistivity measurements, known as Automated-ERT (A-ERT) or ERT monitoring, offer the ability to track the ongoing evolution of permafrost and capture rapid, heterogeneous and non-linear changes in its temperature and ice content (*e.g.*, Scandroglio et al., 2021; Doetsch et al., 2015). A-ERT over period of several years has been recently used to track the degradation of permafrost associated with global warming (Mollaret et al., 2019; Keusching et al., 2017; Doetsch et al., 2015; Hilbich et al., 2008).

Furthermore, the time-lapse inversion of geophysical data derived from fixed monitoring network provides a succession of tomograms showing the spatial and temporal changes in subsurface resistivity (see; Karaoulis et al., 2013; Loke, 1999). The results of time-lapse inversions of apparent resistivity data can be directly linked to the evolution of permafrost throughout the annual cycle or to rapid variations caused by water infiltration or drainage during short periods of time (Keusching et al., 2017; Hilbich et al., 2008).

That said, A-ERT at high altitudes (>3500 m) and over a multi-profile setting has not yet been tested for pluriannual permafrost monitoring. The use of A-ERT under high-altitude conditions presents specific challenges due to extreme topographical and climatic conditions as well as meteorological events. However, it could provide valuable information about the hydrogeological system and the evolution of permafrost in environments where its distribution and dynamic are highly heterogeneous.

In this study, we present the results of an A-ERT survey conducted over nearly four years (2020-2023) at Aiguille du Midi (AdM) in the Mont-Blanc massif (French Alps). The site consists of massive and fractured granite and includes infrastructures such as tunnels and elevators. Water infiltration was observed at various locations within the tunnels. The objective

of this study is to investigate permafrost dynamics from infra-seasonal to multiyear timescales and through various rock faces of a same site. Our goals include: (1) evaluating the potential of A-ERT to characterize permafrost dynamics, its heterogeneity and non-linearity in steep alpine rockwalls; (2) assessing the accuracy of temperature derived from resistivity measurements; and (3) studying the hydrogeological system, including water infiltration and drainage in fractures, along with their thermal impacts. For this objective, a total of three profiles were deployed downwards from the summit in three directions: North-West (NW), South (S) and East (E). Each profile consists of 32 electrodes spaced at 5 m. In addition to field data, laboratory resistivity measurements were conducted on granite core sample, in both unfrozen and frozen conditions. Furthermore, temperature which was continuously monitored in a 10 m deep borehole along the NW profile is used to quantitatively evaluate the temperature estimation using geophysical measurements of electrical resistivity.

2. Study site

We investigate the Aiguille du Midi (3842 m a.s.l.), which is the highest and most western summit of the Aiguilles de Chamonix (Fig. 1a). It is located on the NW flank of the Mont-Blanc massif. It includes three peaks that are all connected by human-made bridges and galleries. In average, AdM is visited in summer by around 5000 visitors a day transported from the city of Chamonix by cable-cars. The appearance of the summit of AdM has been greatly affected by the construction and developments carried out since the 1950s (see Fig. 1). Our study focuses on the central peak, which is the highest among the three, and which hosts the cable-car station connecting AdM to Pointe Helbronner with the *Panoramic Mont-Blanc* cable car. The topography is characterized by vertical rock walls with an average slope of 78° on the North-West face.

The lithology in the study area is dominated by massive granite with a very low porosity (~ 0.01, Magnin et al., 2015a). The highest parts (3740 to 3840 m a.s.l.) of the peak tend to be

steep, contain few large fractures, and, in places, are characterized by vertical foliation bands and small cracks (Magnin et al., 2015b). Figure 2 shows the mean monthly and annual air temperature at AdM during the study period. The year 2021 was the coolest year (yearly averages: -5.8 °C, -6.9 °C, -5.3 °C, and -5.7 °C from 2020 to 2023, respectively).

In order to evaluate the thermal state and the distribution of permafrost at AdM, three boreholes have been drilled in 2009. They are labeled BH-NW on the NW face, BH-S on the South face and BH-E on the East face. Each borehole is 10-m-deep and 66 mm in diameter, and was drilled normal to the topography (their position is shown in Fig. 1b-d). Each borehole is equipped with 15-thermistor strings calibrated in an ice-water bath and then placed at different depths in the borehole. The temperature of the permafrost core shows significant variability from one face to another. For example, at a depth of 10 meters, the temperature is approximately -4 °C on the NW face, while it is around -1 °C on the sun-exposed S face (Magnin et al., 2024). These temperature differences indicate the presence of strong temperature gradients within the rock mass. In the same way, the Active Layer Thickness (ALT, *i.e.*, the maximum seasonal thaw layer) is also highly variable as interpolated between temperature sensors: it is observed to be around 1.3 to 2.7 m in summer on the NW side, while it reaches 4.8 to 7.6 m on the S side in the early fall. Below this depth, permafrost is present (Magnin et al., 2024). Figure A1 (appendix A) shows the temperature variation over depth in boreholes BH-NW and BH-S on different date.

BH-NW is located along an electrical resistivity profile (NW profile) and is positioned between electrodes 8 and 9 (counted from the bottom) of the NW profile (see Fig. 1c). The temperature measured in this borehole is used to assess the accuracy of the temperature derived from ERT results using the petrophysical model presented in the next section.

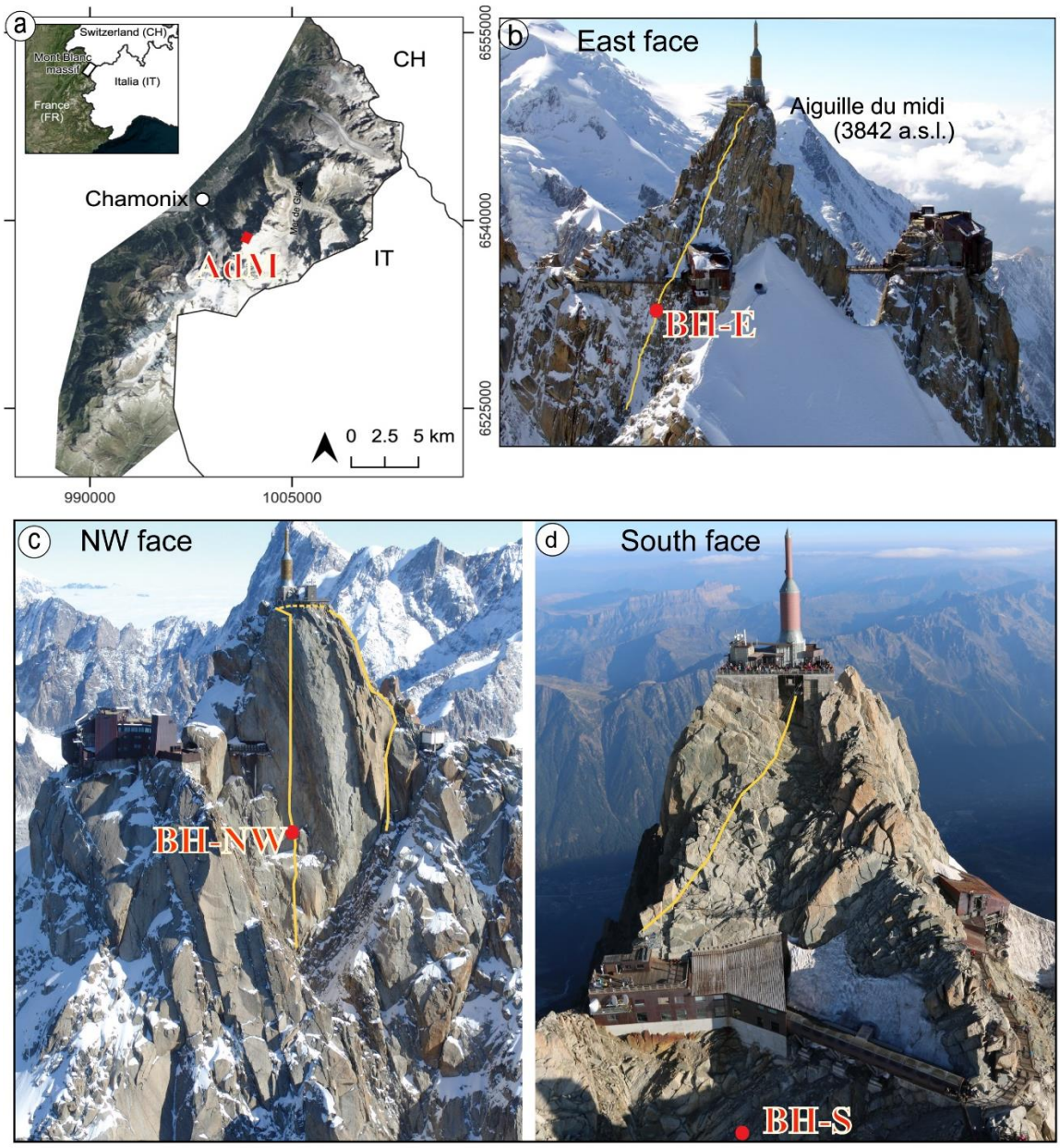

Figure 1. Study site location and geophysical survey setting. The yellow lines indicate the approximate positions of electrical resistivity profiles on each side (NW, E and S profiles). The red dots denote the borehole locations. (a) Location of the study site (Aiguille du Midi (AdM)), in the Mont Blanc massif (here, the French side)). The electrical resistivity profile and borehole locations at the East face(b), at the North-West face (c) and at the South face (d).

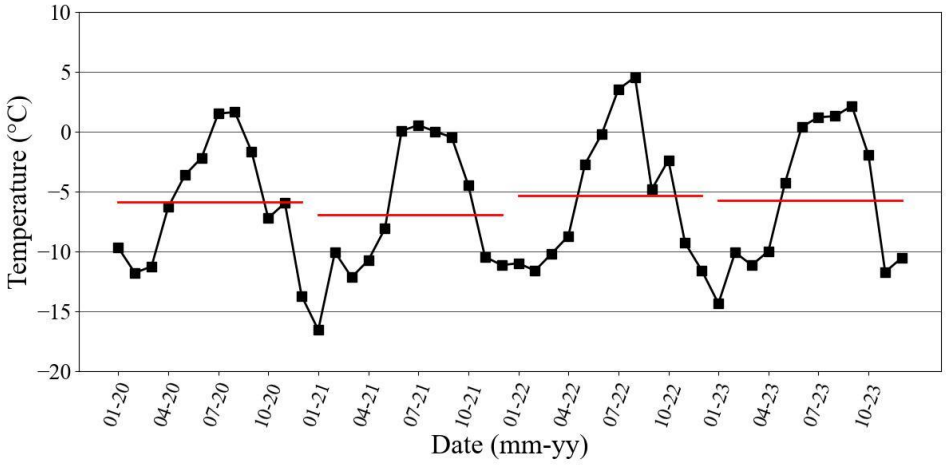

183

184 **Figure 2.** Monthly average air temperature (°C) at AdM during the survey period (Data from the
185 meteorological station of Institute of Environmental Geosciences at the Aiguille du Midi). Horizontal
186 bars show the annual average air temperature.
187

188 ## 3. Electrical conductivity - temperature relationship

189 The electrical conductivity of a rock represents its ability to conduct an electrical current
190 under the application of an imposed electrical field. The electrical conductivity (inverse of the
191 electrical resistivity) of a rock depends on its porosity ϕ (dimensionless), water content θ
192 (dimensionless), pore water conductivity, Cation Exchange Capacity (CEC), and rock
193 temperature T (in °C) (*e.g.*, Revil et al., 1998).

194 Above the freezing point (typically, but not necessary, around 0°C), electrical
195 conductivity ($\sigma(T)$ in S m^{-1}) increases linearly with temperature according to Revil et al. (1998):

196 $$\sigma(T) = \sigma(T_0)\left[1 + \alpha_T (T - T_0)\right], \qquad (1)$$

197 where α_T = 0.021±0.02 °C^{-1}, T_0 = 25°C denotes the reference temperature, and $\sigma(T_0)$
198 denotes the conductivity of the rock at the reference temperature.

199 In contrast, under freezing conditions, temperature variations have a significant
200 influence on electrical conductivity because of the occurrence of an insulating phase (*i.e.*, ice
201 formation) in the pore space and despite the increase in the salinity of the pore water with

temperature decrease. This temperature dependence of electrical conductivity can be modeled as follows (see details in Duvillard et al., 2021; 2018; Coperey et al., 2019):

$$\sigma(T) \approx \left[(\phi - \theta_r) \exp\left(-\frac{T - T_F}{T_C} \right) + \theta_r \right] \frac{\sigma(T_0)}{\phi} \left[1 + \alpha_T (T - T_0) \right], \quad (2)$$

Where θ_r (dimensionless) denotes the residual water content when T<<T_F, T_F denotes the liquidus or freezing point/temperature, T_C denotes a characteristic temperature controlling the transition between the unfrozen state and the frozen state, and $\phi - \theta_r$ denotes the maximum volumetric ice content at low temperatures. Equation (2) provides the opportunity to convert electrical conductivity or electrical resistivity tomogram measured in the field to a temperature distribution (*e.g.*, Duvillard et al., 2021).

4. Methods

4.1 Laboratory measurements

In order to calibrate our field measurements and evaluate the parameters (*e.g.*, T_C, θ_r) in the petrophysical model discussed above (Section 3), we conducted an electrical conductivity experiment on a granite rock sample collected from an outcrop on the site. The cube-shaped granite sample (dimensions: 5×5×5 cm^3) was dried during 24 h at approximately 100 °C, then saturated under vacuum with degassed water. The water conductivity was measured to be 0.016 S m^{-1} (representative of the conductivity of collected water from the field (about 150 µS/cm or 0.015 S m^{-1})) at equilibrium at T = 25˚C. The sample was left in the solution for several weeks to reach chemical equilibrium before performing the laboratory measurements. The Sample was characterized by a very low porosity ϕ = 0.014.

For thermal-resistivity analysis, the sample was placed in a heat-resistant insulating bag immersed in a thermostat bath (KISS K6 from Huber; dimensions: 210×400×546 mm^3; bath volume: 4.5 L). The temperature of the bath was controlled with a precision of 0.1 °C. Glycol

was used as the heat carrying fluid (Coperey et al., 2019). The complex conductivity spectra were obtained over the temperature range of +10 to −10 °C, using a high-precision impedance-meter ZEL-SIP04-V02 (Zimmermann et al., 2008). The resistivity measurements reported here are at a frequency of 1 Hz (Coperey et al., 2019).

Figure 3 presents the measurement results for the granite sample from the study site (labeled Sample AdM), alongside measurements of another granite sample (Sample Cosmiques) collected from a nearby site at the lower Cosmiques ridge (Mont-Blanc massif, 3613 m a.s.l.), as reported by Duvillard et al. (2021). The experimental datasets are presented along with data fits, using Equations 1 for temperatures above the freezing point, and Equation 2 for temperatures below the freezing point. We see that the model proposed in Section 3 is able to fit the data above and below the freezing temperature, providing a proxy for connecting electrical conductivity or electrical resistivity to temperature.

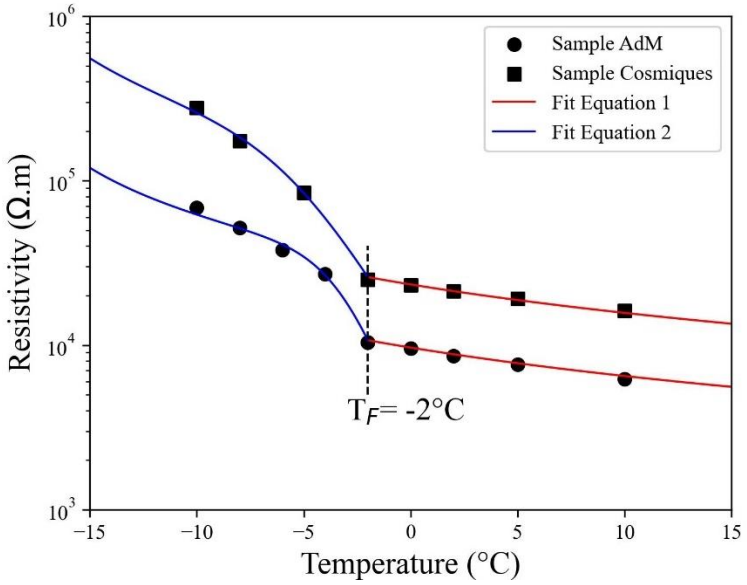

Figure 3. Resistivity-temperature relationship from laboratory measurements on two granite samples from (1) the study site (Sample AdM), and (2) from the Cosmiques ridge, Mont-Blanc massif, West (3613 m a.s.l.) (Sample labeled Cosmiques). T_F denotes the freezing temperature. The solid lines correspond to the fits using the Equation 1 (red lines) and Equation 2 (blue lines), in unfrozen and frozen conditions, respectively. The parameters of the model in Equation 2 are (T_C=-1.3 °C, θ_r=0.004, $\sigma(T_0)$ =

245 2.3×10^{-4} S m^{-1}) for Sample AdM, and (T_C= -2.17 °C, θ_r = 0.004, $\sigma(T_0)$ = 9.5×10^{-5} S m^{-1}) for Sample
246 Cosmiques.
247

248 **4.2 ERT Data acquisition**

249 ERT has been conducted over a four-years period (06/2020 - 12/2023). A total of three
250 cables, each with 32 take-outs spaced 5 m (for a profile length of 155 m), were installed. The
251 three cables were deployed downwards from the summit in three directions: North-West (NW),
252 East (E) and South (S). The S profile starts at the South side and pass to the North-West side
253 around mid-distance (see Fig. 1c, d). The installation of cables was gradual (over a year) starting
254 from NW side (installed in June 2020), then on the South side (installed in July and August
255 2020), and finally on the East side (installation finished in March 2021 because of snowpack in
256 2020 at this side). In order to ensure good electrical contact between electrodes and rock mass,
257 stainless steel (A4/316) climbing bolts (Fischer 10×126 mm) poured in salty bentonite were
258 used and placed firmly in holes drilled in the rock. A specially designed jumper was used to
259 attach each take-out to the bolt to ensure maximum contact. The resistivity cables were attached
260 to anchors to minimize damage from rockfall and snow pressure.

261 A LS2-Terrameter (ABEM) with internal impedance of 20 MΩ was used for the data
262 acquisition. The ERT device and control system for monitoring were deployed inside the
263 summit station with network access, power connection, and overvoltage protection. Data
264 acquisition was fully automated and remotely controlled. Finally, the position of every electrode
265 was measured using a differential GPS when the signal is available and a theodolite in steep
266 areas. The measurements were carried out using a Wenner configuration, which provides a high
267 signal-to-noise ratio and is widely used in mountain permafrost environments (Mollaret et al.,
268 2020; Krautblatter and Hauck, 2007; Dahlin and Zhou, 2004). Each profile consists of 155 data
269 points. An injected current ranging from 0.1 mA to 200 mA was applied, with a maximum stack
270 numbre of 4 was applied to ensure a standard deviation of less than 5 % in the measured

resistivity. The first measurements were performed in June 2020. In the period June 2020 and September 2021, ERT measurements were repeated occasionally. Then the continuous measurements started in late September 2021 after developing an automated system of acquisition. Datasets were daily recorded for each profile (NW, S and E profiles).

A Contact Resistance (CR) test was performed before each series of measurements. A high contact resistance in the rock wall (>100 kΩ) was encountered throughout the entire survey period, which posed a challenge to the quality and continuity of data acquisition. CR varies between a few kΩ and 10 000 kΩ. However, beyond a CR threshold, the ERT measurements lose their accuracy. Electrodes with high CR (>600 kΩ) are excluded automatically by the LS2, leading to gaps in the pseudo-section of apparent resistivity. Special efforts were made to reduce CR and improve the electrode/rock contact, including the addition of salty water, using copper electrodes and duplicate electrode. The latter one resulted in a significant and a durable improvement in RC (one order of magnitude reduction in CR). Figure B1 shows the temporal evolution of CR at profiles S and NW and the gaps in the A-ERT measurements.

The A-ERT ran into numerous software and hardware issues, resulting in unsystematic data gaps. The E face cable was severely damaged by a lightning strike, before being totally destroyed by an uncontrolled rock purge. Additionally, NW and S cables were both damaged by rockfall, leading to significant data gaps (see Fig. 4). Repairing or replacing the damaged cables was not possible for several reasons (e.g., limited access to the cable path because of accumulated snowpack).

4.3. Data processing and inversion

The apparent resistivities were calculated using the open-source package pyGIMLI (Rücker et al., 2017), which combines measured resistances and electrode positions. Figure 4 shows the temporal distribution of apparent resistivities measured and the averaged apparent resistivity along the S-profile, with examples of time series (shown in different colors) of

measured apparent resistivities obtained using various quadrupole configurations (AMNB). The majority of measured apparent resistivities are distributed over three decades (100 Ω.m to 100 kΩ.m), with few data points out of this range.

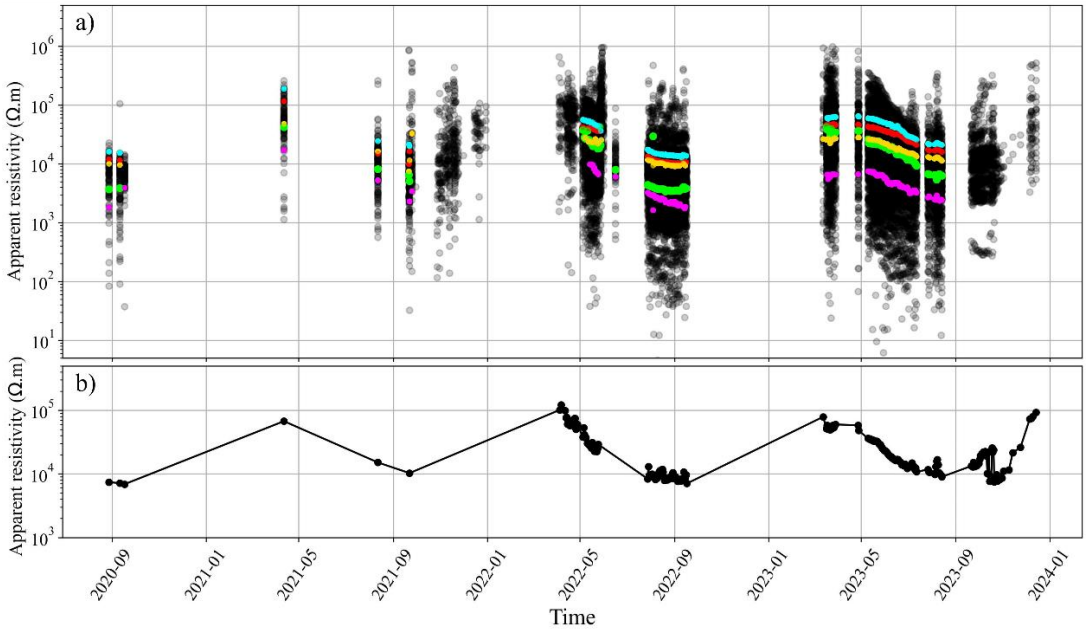

Figure 4. Distribution of measured apparent resistivity. a) daily distribution of the apparent resistivity over time at the S face (approximately 300 datasets). Colored lines present examples of resistivity times series, each corresponding to a different set of quadrupoles (AMNB). b) Mean daily measured apparent resistivity at the S face.

For datasets used in inversion, the selected data were subjected to the following analysis. The primary criterion was the number of connected electrodes. We tolerated up to four unconnected electrodes (because of high RC) in a pseudo-section depending on their positions, as the contribution of electrodes is not equal in the pseudo-section. After selecting valid datasets, outliers within each pseudo-section were removed. For data filtering, we analyzed individually few pseudo-sections (at different times (summer, spring), as a result of this analysis we decided to apply filter outliers out of range (300Ωm - 20 kΩm) for data measured in summer and autumn, and out of range (300Ωm - 200 kΩm) for data measured in spring and winter. More data filtered at higher resistivities, where data quality is usually poor. Table 1 appendix C

summarizes the data presented in this study. Most datasets have more than 80 % of the original recorded data points of each pseudo-section.

The inversion of the electrical resistivity datasets was performed using the open-source package pyGIMLI (Rücker et al., 2017; Günther et al., 2006). The inversion uses a Gauss-Newton minimization algorithm of a cost-function penalizing the roughness of the electrical resistivity distribution on an irregular grid (Günther et al., 2006). In the absence of reciprocal dataset to estimate errors in measurements, we used a linear error model which assumed 5 % relative error and absolute error 1e5. The parameters used in the inversion process are zWeight = 10 and smoothness (lambda) =1. The inversion parameters zWeight was chosen higher than 1 to enhance the vertical discontinuities and structures (i.e., the active layer, infrastructures), during the inversion process. Then, an iterative process was conducted to select the smoothness parameter that minimizes the data misfit of individual inversions of a reference dataset.

5. Results and interpretation

5.1. Overview of the raw data

Our interpretation of the ERT data starts with an analysis of the measured apparent resistivity data, which can provide insights into subsurface conditions. Figure 5 shows the variations in the average apparent resistivity associated with the same electrode distance or pseudo-depth for three selected datasets from two profiles (NW and S profiles). The data reveal the interannual and seasonal variations in the measured apparent resistivity, as well as the differences between the two sides. During frozen conditions at the surface (dataset from 12-04-2021), the apparent resistivity is almost the same on both sides (~100 to 120 kΩm near the surface), with only a slight decrease with depth at both sides. At the end of summer (dataset from 17-09-2021 and 25-09-2021), the resistivity values are higher in 2021 than in 2020 on both sides, which correlates with climatic data indicating that 2021 was a cooler year (see Fig.

2). Secondly, on the north face, the average resistivities increase with depth (from ~7 kΩ.m to ~12 kΩ.m), while on the south side, the average resistivities decrease with depth (approximately 13 kΩ.m at shallow depth to ~7 kΩ.m at greater depth). This difference in the trend between both sides could be interpreted by cooler conditions (permafrost at shallow depth) at north side and warmer conditions with thicker active layer at the south face.

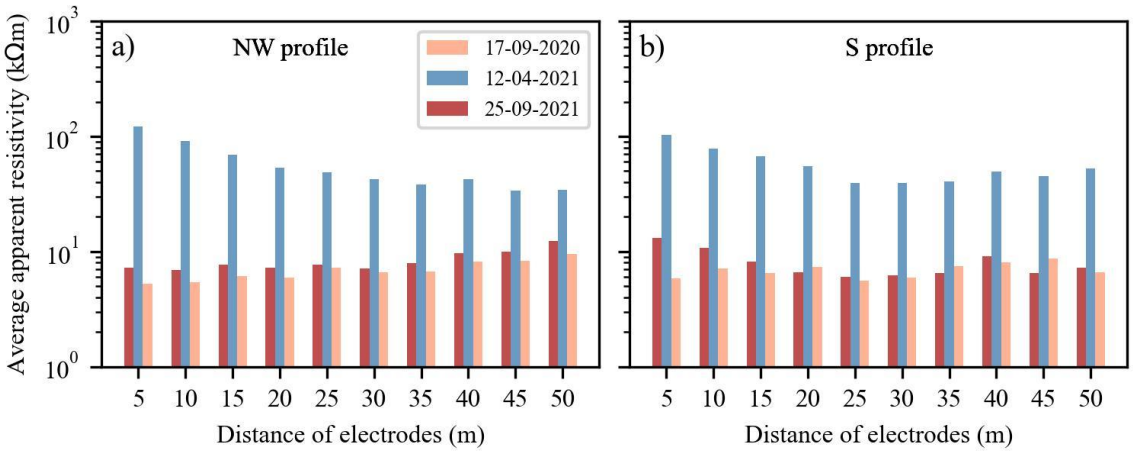

Figure 5. Seasonal variations of the average apparent resistivity at different electrode distances (*i.e.*, at varying depths of investigation). Data in spring show the same pattern on both sides. In autumn, there is a divergence in the trend of average resistivities with depth on both sides, that is related to the hydrothermal conditions at each side.

5.2. Internal structure of the site

In order to gain an overview of the internal structure of the study site based on the resistivity distribution, we carried out inversions of two long profiles (NW+S and NW+E). Figure 6 shows the electrical resistivity tomogram from late summer 2020 (August 26th, 2020), where acquisition on both North-West and South sides (NW+S) was performed. The tomogram clearly reveals the site's internal structure, with low resistivity areas (warm-colored zones) indicating the relative positions of the infrastructure elements (elevator and galleries on both sides). It also shows the extent of the active layer (moderate resistivity areas near the surface), as well as the permafrost evidenced by high resistivity areas (represented in cool-colors).

Although the lower part of the tomogram appears similar on both the NW and S profiles, which is expected since they lie in rockwalls that are alike regarding slope and aspect (where the lowest part of the S profile is deployed on the NW face as well, see Fig 1c), significant differences are evident in the upper part (*i.e.*, above the gallery level), revealing the contrast between sun-exposed (S side of fractured granite and exposed to strong insolation and shaded face (NW side of massive granite mostly dependent on the sensible atmospheric heat flux). The upper part of the profile therefore reveals strong thermal gradient typical of high-alpine summits (Noetzli et al., 2007; Magnin et al., 2017). The high-resistivity area thus appears limited, likely due to the heat flux from the sun-exposed and warm face towards the close shaded-face.

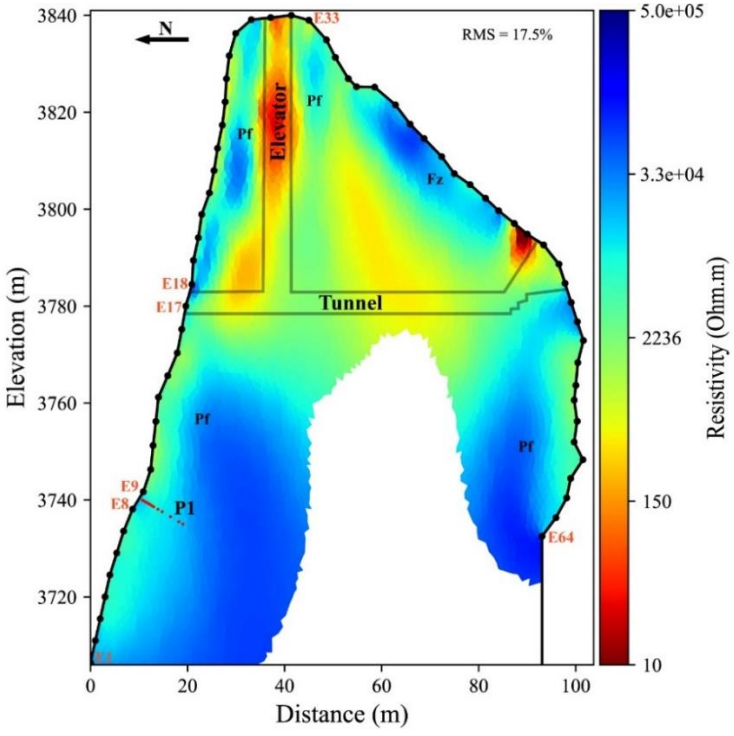

Figure 6. Electrical resistivity tomogram over the NW+S profile measured on August 26, 2020. Grey lines indicate the approximative positions of infrastructure (galleries and elevator). Pf stands for Permafrost zone and Fz for Fractured Zone. E1 to E64 are Electrode numbers. Red dots at P1 indicate the positions of the thermal sensors in BH-NW.

Figure 7 provides an example of the resistivity tomogram for the combined NW and E profiles. This tomogram highlights the changes in resistivity associated with permafrost, active layer,

and anthropogenic installation (such as the elevator and gallery (relatively far from the profile at the E side compared to S profile)). On the eastern side, a thick active layer (> 5 m depth) is observed, with some resistive zones near the surface. These resistive zones are likely fractured zones creating an unsaturated and air-filled zone, and surrounded by moderate resistivity regions where fractures are closed or where water drainage is weak or absent. Data acquisition on the Eastern side (E profile) encountered numerous challenges related to contact resistance, rockfalls and cable connections, resulting in long gaps and insufficient data for long time analysis or time-lapse inversion.

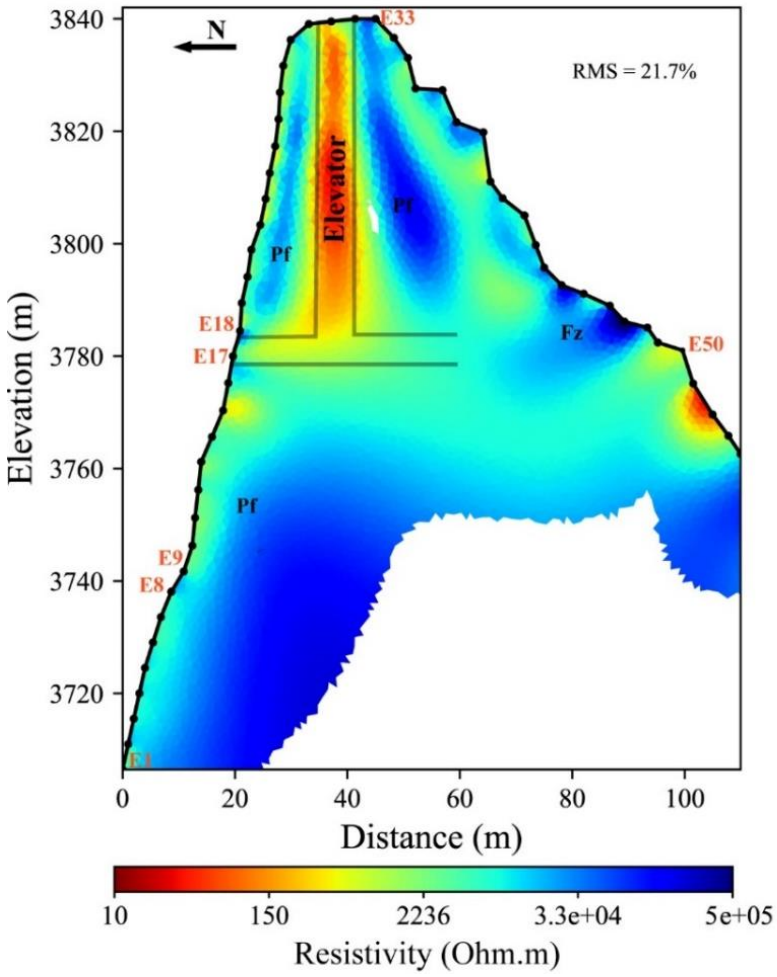

Figure 7. Electrical resistivity tomogram over the profile NW+E at the end of summer (September 25, 2021). Data acquisition on the East profile run into problems related to electrodes contact and cable malfunction. The last 10 electrodes from the E profile were removed during processing due to connection issues. Pf and Fz stand for Permafrost zone and Fractured Zone, respectively.

5.3. Seasonal and interannual variations

In order to track the seasonal and interannual variations in the permafrost, a time-lapse inversion approach was employed to invert datasets for each profile (NW, S). The reference model was moved along with the inversion so that the difference to the preceding step is constrained. Figure 8 shows the tomograms of resistivity distribution after a time-lapse inversion of datasets from NW profile at different time intervals. Spatial and temporal changes in resistivity could be observed, while the anomaly related to the gallery (the warm-colored area (low resistivity area)) remains consistent over time. The permafrost identified by high resistivity, is observed in two zones, above and below the gallery. According to temperature analyzes conducted by Magnin et al. (2024), 2021 was cooler than both 2020 and 2022 (see Fig. 2). This is reflected in the tomograms by a more prominent cool-colored zone (indicating colder conditions) in 2021 compared to data in 2020 (Fig. 8b and d). Additionally, there is a significant variation in the lower part of the tomograms in 2022 (Fig. 8e), which may be related to water infiltration in fractures that shortcut the heat transfer from the surface to depth (Hasler et al., 2011). However, this area is uncertain, as it is located at the border of the tomogram where sensitivity is low. In addition, the RMS error is high in this tomogram, indicating high uncertainties. Therefore, this information should be carefully considered and verified with further measurements focused on the zone of interest. Unlike Offer et al. (2025), no evidence of water accumulation was observed from the geophysical measurements on the NW face. It is suggested that the water table lies at lower altitude (Magnin and Josnin, 2021).

Instead of analyzing temporal resistivity changes in absolute terms, Figure 8 (f - i) illustrates the resistivity variation ratio between two subsequent measurements. This approach facilitates the tracking and visualization of small changes in resistivity. A value of 1 (represented in white color) corresponds to no change in resistivity between the two measurements (reflecting consistent geological conditions, topographic effects, infrastructure

or no considerable change in temperature over time), while the blue color indicates that the resistivity increased over time, and the red color represents the inverse. It can be observed that seasonal variations are the most pronounced, as illustrated in Figure 8g, h and i, compared to short-term fluctuations (see Fig. D2). The effects of freezing and thawing are marked by maximum variations near the surface (in the active layer). In contrast, over a short time interval (i.e., a few weeks), only minor variations are noted (*e.g.*, Fig. 8f, Fig. D2 b, e and j). The decrease in resistivity near the surface at approximately 3780 m, observed in Figure 8i, could be related to water flow around the gallery, where water infiltration occurs every summer, as noticed by local staff (personal communication). Consequently, a specific water diversion system has been installed to protect tourists from these water flows.

Extended times lapse inversion of datasets from NW and S face are presented in appendix D.

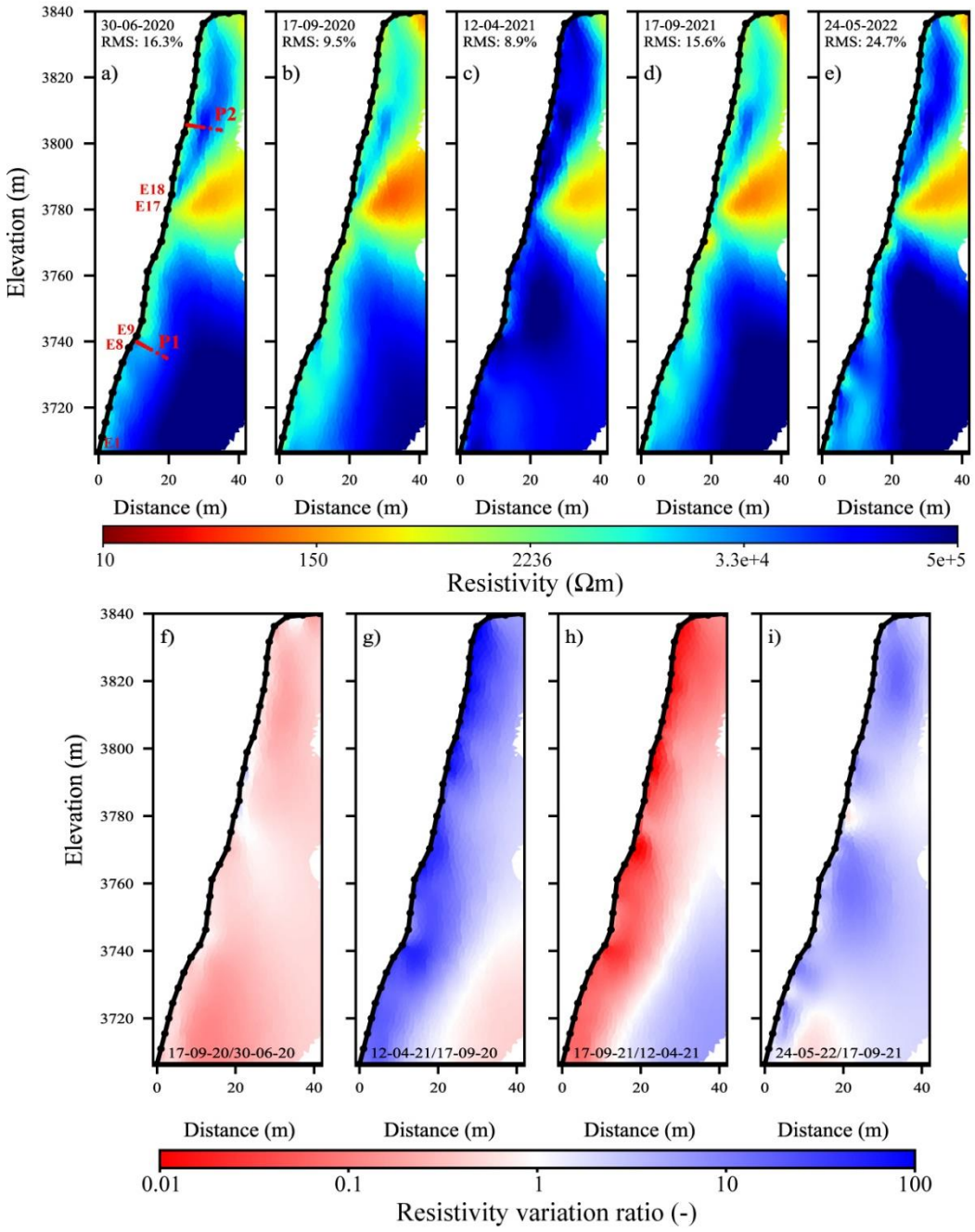

Figure 8. Seasonal and interannual variations of electrical resistivity at NW side. a - e) electrical resistivity tomograms at different dates (from June-2020 to June-2022). The conductive zone (in warm colors) denotes the presence of the gallery and elevator (see Fig. 6). The red dots (P1 in panel a) indicate the positions of the thermal sensors in the borehole BH-NW. Data presented on Figures 9, 10 and 11 are extracted at the red dots (P1 and P2). f - i) resistivity variation ratio between consecutive electrical resistivity tomograms. Blue colors indicate an increase in resistivity, while red colors represent a decrease in resistivity from one measurement to the next.

Inverted resistivities at P1 (BH-NW) and a virtual borehole at P2 are presented in Figure 9. The extracted resistivities show that the variation of resistivity with depth is more pronounced at P2. This greater variation could be due to a higher water content in the active layer or a thicker active layer at P2 compared to P1. The greater thickness of the active layer in the upper section can be explained by the 3D heat transfer and the proximity of the shaded face (NW side) to the sun-exposed faces (S side) in the top part (Magnin et al., 2017;). Additionally, the presence of the elevator contributes heating and cooling the granite from inside. In the lower section (profile P1), the contrast between the resistivity in the active layer and that in the permafrost is not significant, possibly due to low water content (porosity is around 1 %), or high surface conductivity in granite. However, it is important to note that the ALT is about 2.7 m at the end of summer (from BH-NW measurements, see Fig. A1), and the smallest quadrupole spacing is 15 m, which is insufficient to capture thin variations close to surface (Edwards, 1977). Additionally, there is a slight decrease of resistivity over time in the permafrost from June 30, 2020 to June 30, 2022. Finally, in 2021, resistivity values were higher in both the upper and lower parts compared to 2020 and 2022, a trend that aligns with temperature measurements (see Fig. 2, or details in Magnin et al. (2024)).

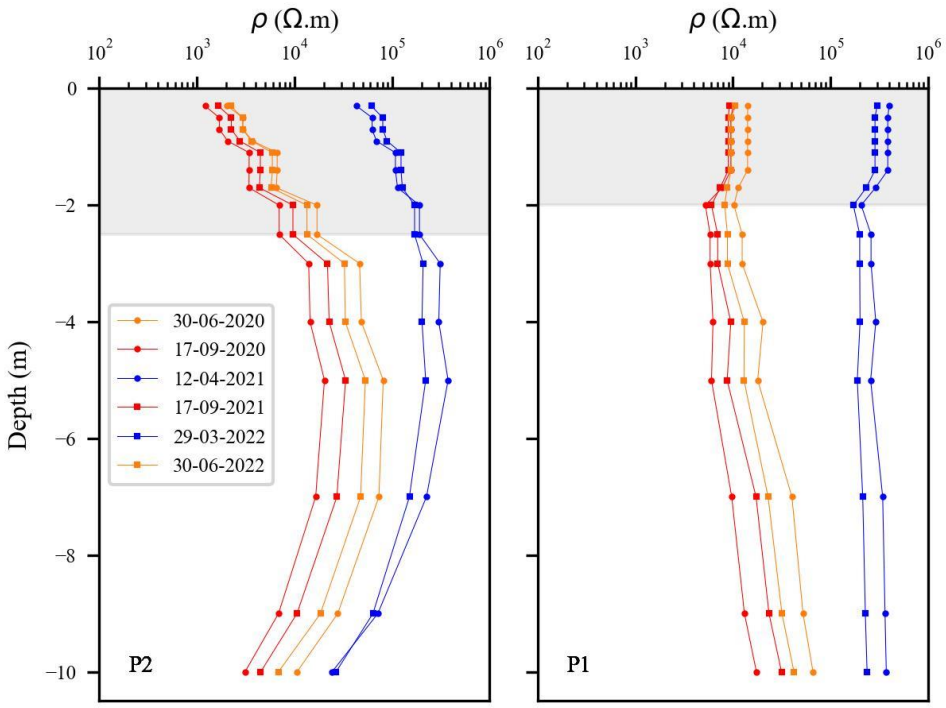

Figure 9. Resistivity extracted over depths at different dates and locations (P1, P2). Resistivities extracted from tomograms in Fig. D1. There is greater variation at the higher profile (P2), where heat transfer from the nearby sun-exposed faces is more significant in the site's upper part.

5.4. Temperature - resistivity relationship

Extracted resistivities at P1 are superimposed on borehole BH-NW, where temperature measurements are available. We are using these two datasets (*i.e.*, temperature and resistivity measurements at the same location, BH-NW) to explore the potential for estimating temperature based on electrical resistivity measurements and to perform a quantitative evaluation of the T-R relationship determined in a laboratory.

It is known that, when temperature > 0 °C (*i.e.*, the case in the active layer), resistivity depends on multiple variables, including porosity, water content, water salinity, Cation Exchange Capacity (CEC) and temperature (Revil et al., 2018), which makes it difficult to model or predict the resistivity value in the active layer. In contrast, under frozen conditions, resistivity of a medium is primarily controlled by the remaining unfrozen pore water content, and is assumed to be dependent on temperature, while the other parameters remain constant.

Therefore, the extracted resistivities in the frozen zone were converted to temperature using the petrophysical model in Equation 2 (Duvillard et al., 2021; 2018; Coperey et al., 2019). Figure 10 shows the measured temperature alongside the estimated temperature from ERT data, plotted against depth at different dates (in summer and autumn). A good agreement can be observed between the measured and estimated temperature in frozen conditions, with differences of less than ±1 °C at depths between 4 and 10 m. This suggests that temperature distribution across the site can be calculated using this model (e.g., Duvillard et al., 2021), assuming the medium is homogenous and resistivity variations are solely attributed to temperature. However, at AdM, this condition is not satisfied due to the infrastructure, which creates a conductive zone within the medium (see Figs. 6, 7). Predicting temperature in the active layer is not feasible since temperature is not the dominant factor affecting resistivity. The data collected under frozen conditions at the surface (*i.e.*, measured in winter and spring with high contact resistance) resulted in large discrepancy between the estimated and measured temperature and could not be reliably used for temperature estimation. A-ERT measurements still a challenge in frozen condition at surface.

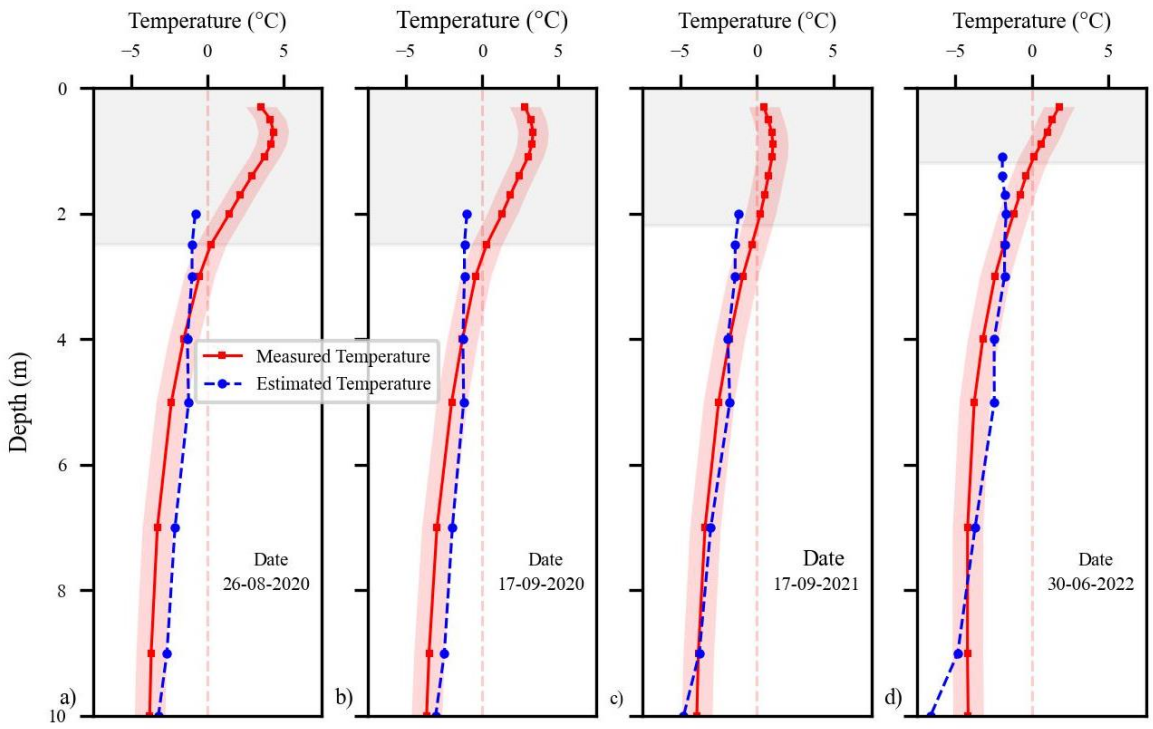

Figure 10. Comparison between measured temperatures in BH-NW and estimated temperatures derived from geophysical measurements (*i.e.*, extracted resistivity values at different dates) using the petrophysical model in Equation 2. The gray-shaded area indicates the extent of the active layer at the time of measurement. The red-shaded zones show the ±1 °C range around the measured temperature.

To go further in our analysis, Figure 11 shows the extracted resistivity at P1 vs. temperature data measured in BH-NW at different dates. Laboratory measurements on two granite samples (labeled Sample AdM and Sample Cosmiques) are also shown. Three key observations can be made: i) Data collected in winter and spring (frozen conditions at surface), presented by blue symbols, show resistivity values higher than those expected from laboratory measurements, which aligns with the field observations reported by Maierhofer et al (2024). This may be related to the salt segregation during freezing, which may enhance conductivity of pore water and, consequently reduce resistivity of samples. ii) At higher temperature (unfrozen conditions at surface), a linear trend is observed that aligns with laboratory measurements for part of datasets. The difference in resistivity between field and laboratory data under unfrozen conditions could be attributed to the heterogeneity at the field scale and/or the difference in

water content and water salinity between laboratory and field environments. Where, laboratory measurements were conducted in saturated conditions (saturation was performed under vacuum using degassed water). iii) Field data exhibit greater dispersion compared to laboratory data, which can be attributed to several factors, including 3D effects at the site, the influence of infrastructure and heterogeneity at different scales (from fractures scale to pore scale). In addition, there is a difference in resolution between the two field measurements: temperature measurements are local, while resistivity measurements account for a larger volume.

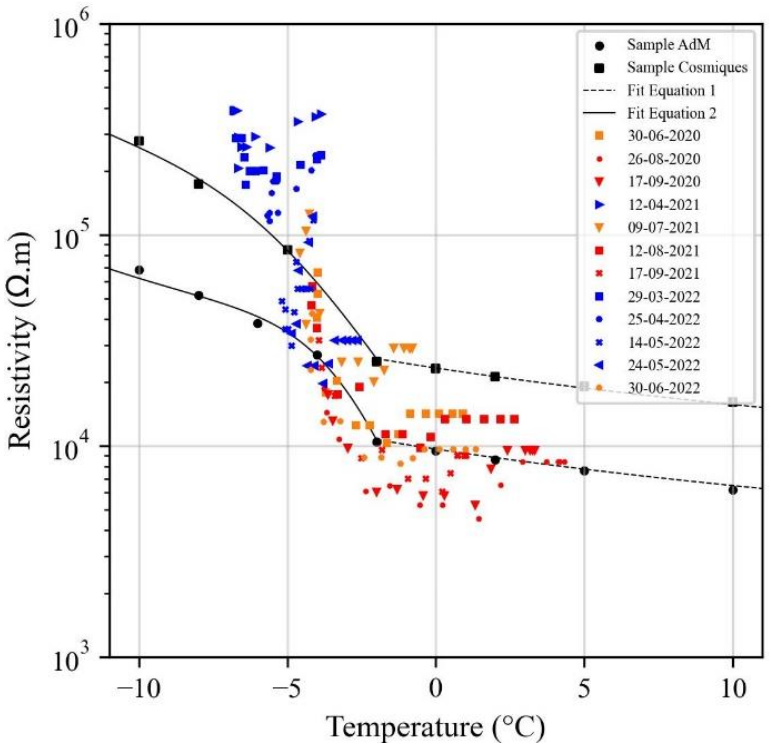

Figure 11. Resistivity vs. temperature. Resistivities are extracted from the tomograms in Figure D1 at location P1. Temperature is measured by sensors at BH-NW. Laboratory data on two granite samples and fitting with Equation 1 and 2 are shown too.

5.5. Hydrogeological dynamics

One of the objectives of this study was to assess hydrogeological dynamics. Due to gaps in the ERT time series, the analysis did not yield conclusive information. Therefore, we selected

specific datasets (nearly complete pseudo-sections) and compared the results of the time-lapse inversion to gather information about water infiltration and drainage. Although we could not precisely identify the infiltration and drainage pathways or the water table (which may be located at a lower altitude) using ERT measurements, we observed several instances that serve as evidence of water flux.

Figure 12 shows the results of the time-lapse inversion of datasets along the S profile at various time intervals. The same inversion parameters were applied as those used on the NW side. In the upper part of the profile (above the gallery), seasonal variations are influenced by fractures, which affect the flow pathways and resistivity signals during seasonal cycle. This part of the profile is characterized by strong insolation (*i.e.*, sun-exposed area) that dries the rock and fractures, leading to an increase in resistivity near the surface due to air-filled pores and fractures (*e.g.*, Fig 12b and e). The decrease in resistivity in this zone (*e.g.*, Fig 12a, c, d and h), could be interpreted as a result of a higher water saturation caused by the circulation of snowmelt or rainfall water. The absence of precipitation data at the site prevented the correlation and validation of the ERT observations with rainfall events. Water infiltration and drainage in this area increase the ALT. The conductive zone observed beneath the fractured area results from minimal or nonexistent water drainage, which leads to higher water saturation.

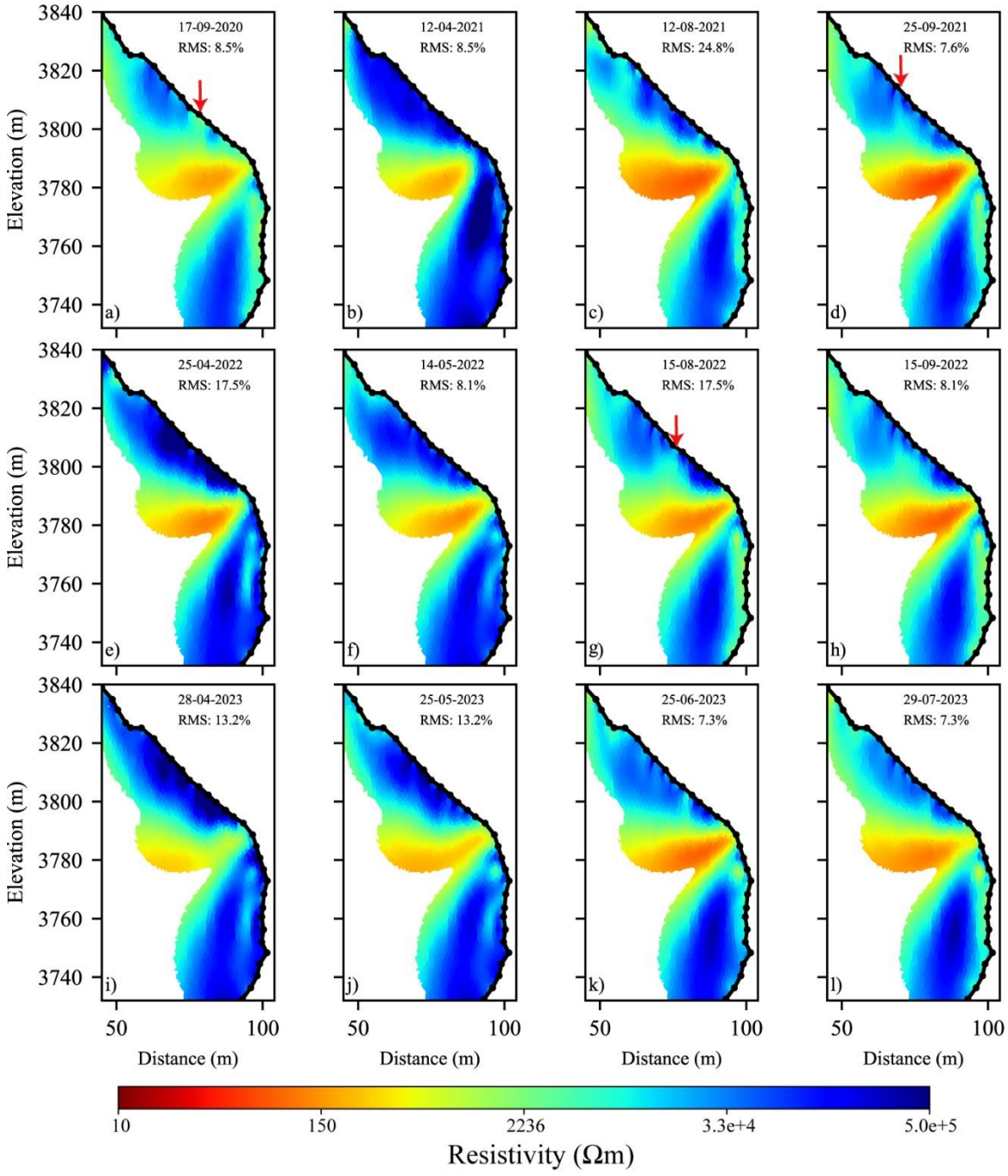

Figure 12. Tomograms of resistivity along the south side (S profile). Electrical resistivity tomograms at different dates (from September-2020 to July-2023). The conductive zone (in warm-colors) explained by the presence of the gallery (see Fig. 6).

6. Discussion

In this study, we use repeated and automated ERT to investigate the evolution of permafrost at a high mountain site. As expected, data from A-ERT are of lower quality compared to manual measurements, where the operator can intervene to improve CR after each electrode check (Doetsch et al., 2015; Hilbich et al., 2009). The high CR is the main problem for getting good and durable A-ERT. Therefore, conducting ERT in frozen surface conditions on rockwall permafrost remains challenging because of the high CR. Various approaches were tested to improve CR. For instance, duplicated electrodes provided a durable and significant improvement in CR (~ one order of magnitude reduction), helping to enhance data quality.

Time lapse inversion of the measured resistivity showed the seasonal and interannual variations (Fig. 8 and 9). We observe that resistivity decreased over time at greater depths (*e.g.*, at P1 and P2, comparing data from July 30, 2020 and July 30, 2022), indicating degradation of the permafrost such as also revealed by borehole measurements (Magnin et al., 2024). However, this decrease in resistivity is minor, likely due to the relatively short observation period of two years at NW side and 4 years at S side. A thicker active layer is observed at the upper section, which can be attributed to 3D heat transfer processes and the close proximity of the shaded north-west face to the sun-exposed southern faces in the upper part of the slope (Magnin et al., 2017; Noetzli et al., 2007). The presence of the galleries and elevator contributes also to heat the granitic peak from inside decreasing the resistivity above the tunnel.

The contrast between the resistivity in the active layer and that in permafrost is not significant in the lower section on the NW side (P1 Fig. 9), which may be due to low ice content/water content where the porosity is around 1 %, or due to high surface conductivity in granite. The alteration of granite involves the transformation of primary minerals (mica and alkali feldspars) into secondary clay minerals (such as kaolinite), which are known for their high cation exchange capacity and, consequently, their contribution to surface conductivity

574 (Piolat et al., 2025; Revil et al., 2024). Additionally, the sensitivity of the used dispositive (with
575 a smallest quadrupole length of 15 m) could affect the resolution of ERT image near the surface
576 (Binley and Kemna, 2005).

577 The temperature estimation based on ERT data leads to good agreement with observed
578 temperatures, with differences of less than ±1 °C at depths 4 to 10m, indicate that the proposed
579 model (Equation 2) can accurately reproduce temperatures in permafrost. Consequently, this
580 approach could provide valuable insights into the thermal distribution at the site. However, the
581 internal temperatures of permafrost typically have just a few degrees below freezing (e.g.,
582 Noetzli et al., 2024). A precision of 1°C may be insufficient in permafrost studies, where minor
583 temperature variations can greatly impact stability and long-term thermal evolution.

584 Furthermore, the transition between frozen and unfrozen conditions is not clearly
585 distinguished at resistivity curve extracted from field measurements (see Fig. 9, 10). The
586 freezing point, which is expected to result in a significant change in resistivity (as observed in
587 laboratory measurements), does not exhibit the same effect in field. However, some datasets
588 show gradual increase in resistivity when temperature decreased (i.e., indicating gradual
589 freezing). This point needs to be addressed in further research with smaller dispositive to
590 improve the resolution of geophysical measurements.

591 On the south face, the tomograms of resistivity show near-surface pore desaturation,
592 attributed to strong insolation on the rock face that is perpendicular to the sun beam, along with
593 features that may relate to water infiltration along fractures. The exact pathways of infiltration
594 and drainage are still ambiguous, possibly due to the resolution of resistivity measurements.
595 Finally, with the AdM setting, we can also hypothesize that the saturated conditions are almost
596 never reached. There is water circulation, but no accumulation or development of a water
597 column, because the water table is likely lower than the area covered by the measurements
598 (Magnin and Josnin, 2021), conversely to Offer et al. (2025) at the Kitzsteinhorn for example.

599 Indeed, our investigation is in a different setting: high altitude peak lying ~2000 m above the
600 water table (Magnin and Josnin, 2021) while in the Kitzsteinhorn outcrops from a glaciated
601 areas with a probably much closer water table. A-ERT acquisition using shorter spacing
602 between electrodes improves the resolution near the surface, and could provide more detailed
603 information about the subsurface.
604

605 ## 7. Conclusions

606 We used repeated and Automated Electrical Resistivity Tomography (A-ERT) to
607 monitor permafrost dynamics over nearly four years at AdM in the French Alps, aiming to
608 better understand the complexities of permafrost behavior in response to climatic variations.
609 The key findings are summarized as follow:

610 - Through detailed analyses of ERT data, we were able to characterize the active layer
611 and identify significant seasonal and multiannual changes in permafrost dynamics.
612 Importantly, we observed that the ALT varied significantly from one face to another
613 in coherence with climate signals and measured temperatures in boreholes. The
614 results underscore the utility of ERT as a promising, non-invasive approach for
615 monitoring permafrost evolution in high mountains, enabling the identification of
616 permafrost
617 - This research demonstrate that temperature can be accurately derived from
618 geophysical measurements of electrical resistivity based on a petrophysical model
619 connecting resistivity to temperature with precision of approximately ±1 °C in
620 permafrost.
621 - Our assessments of the hydrogeological system revealed instances of possible water
622 flow; however, the exact pathways of infiltration and drainage remain unclear.

Although installation of A-ERT system is relatively low costs, it requires substantial maintenance, especially on unstable rockwalls where rockfalls and lightning effects lead to cable problems. This study highlights the urgent need to address challenges related to climate conditions at high-altitudes that affect device performance and contact resistances, in order to enhance the reliability and durability of continuous A-ERT data collection.

Data availability. Data will be made available on request.

Author contributions. FA performed the data analysis, prepared the figures, and wrote the majority of the text. JB contributed to data acquisition, writing, and figure preparation. FM and AR contributed to the design of the ERT survey, as well as data acquisition and discussion of the results. EM, MBA and PAD contributed to the field installation and acquisition, JR conducted and processed the laboratory data, MK contributed to data inversion and discussion, TC provided air temperature data, LR and PD offered additional information about the site. Finally, all authors actively contributed to the preparation of this version of the paper.

Competing interests. The authors declare that they have no conflict of interest.

Acknowledgments. This research is part of the ANR WISPER project (ANR-19-CE01-0018) and the Action Plan on Risks from Glacial and Periglacial Origin (PAPROG) from the French Ministry of Ecological Transition, Biodiversity, Forest, Sea and Fishing. The authors acknowledge the numerous people that helped with the field work: Antoine Chabas, Bruno Galabertier and Raphaël Gallet from the EDYTEM Laboratory, Simon Alesina from the University of Lausanne, Marc Cleriot for help with field work, and Catherine Coulaud from IGE. The authors are also grateful towards the Compagnie du Mont-Blanc that provided access to the site and support.

Appendix A: Temperature measurements in boreholes on different date BH-NW and BH-S

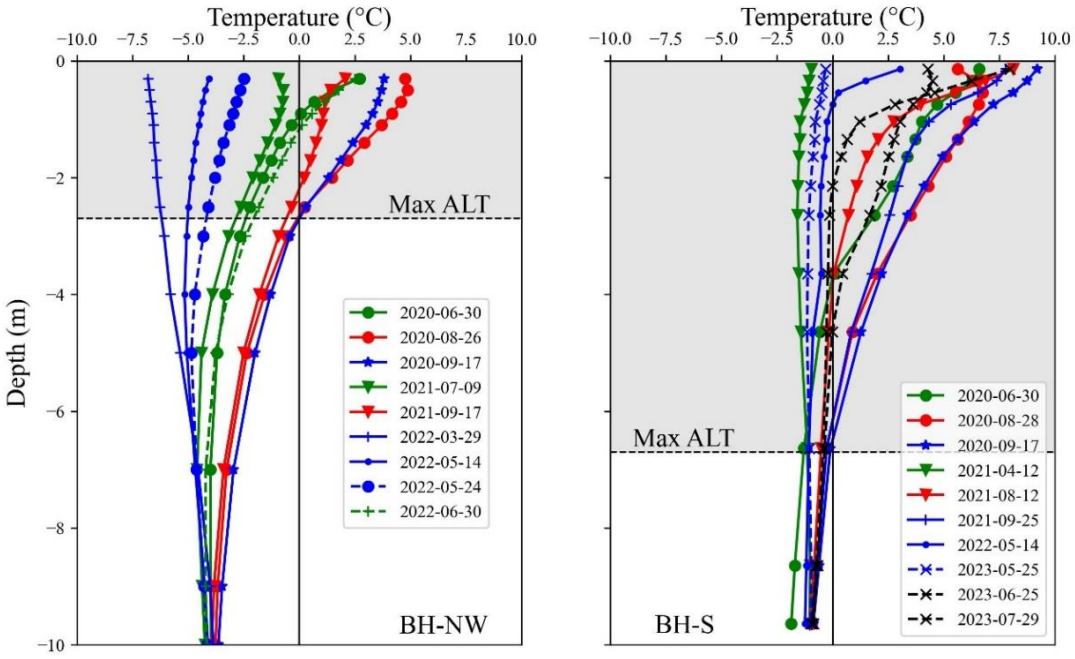

Figure A1: Temperature variation over depth in boreholes BH-NW and BH-S on different date aligned with the ERT measurement periods shown in Figures 8, 12 and D1. The gray-shaded area indicates the extent of the active layer at each borehole.

655 **Appendix B**: Evolution of the contact resistance (CR) over time at NW and S profiles.

656 The CR measured before each daily measurement between 09/2021 and 12/2023 are presented
657 in Figure B1.

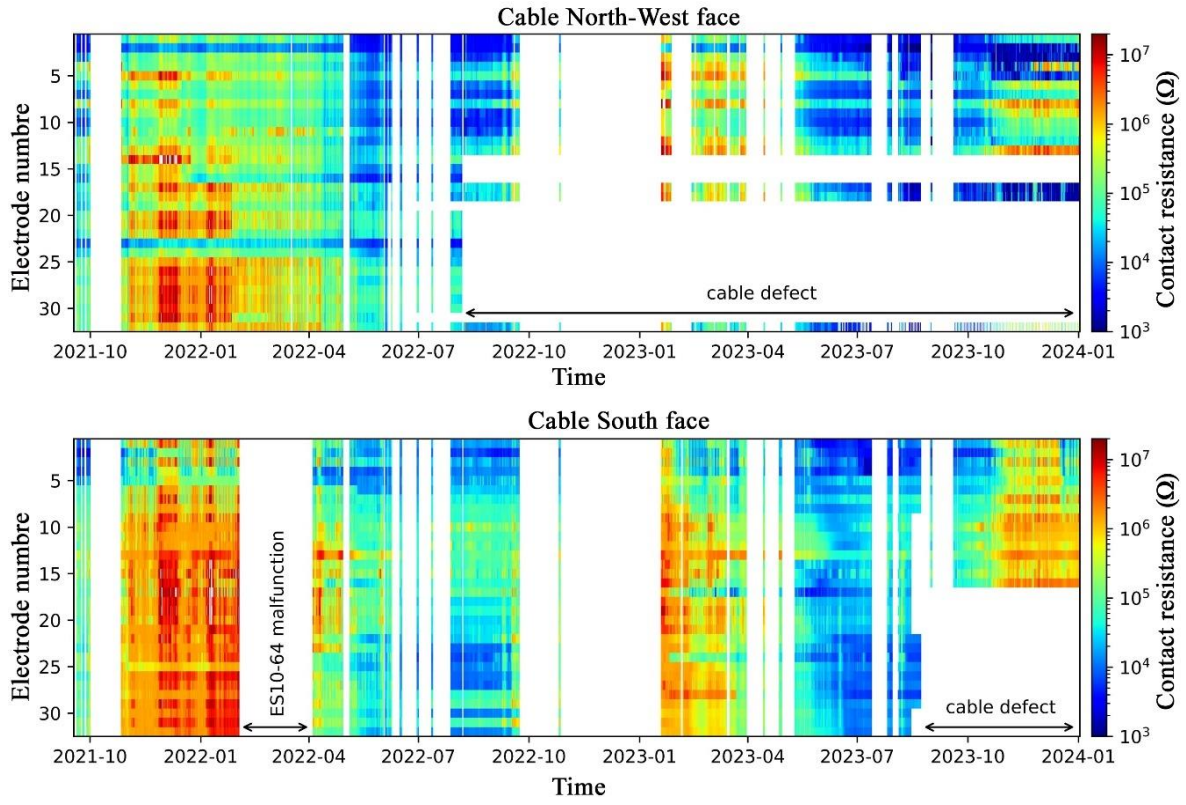

658

659 **Figure B1.** Temporal evolution of contact resistance at the North-West side and South side. Data partly
660 missing are due to cable defects.

661

Appendix C: Summary of data presented in this study

Table 1. Summary of data presented in this study. Number of data before filtering is 155 datum points of Wenner configuration. Most of datasets has more than 80% of total number of measurements. Two datasets have more than 40% of lost data because of disconnected electrodes.

Date	**N-W Profile**		**S Profile**	
	Number of data after filter	Percentage (%)	Number of data after filter	Percentage (%)
30-06-2020	151	97.5	-	-
26-08-2020	149	96.1	90	58
17-09-2020	151	97.5	90	58
12-04-2021	118	76.1	121	78
09-07-2021	114	73.5	-	-
12-08-2021	149	96.1	140	90.3
17-09-2021	145	93.5	131	84.5
25-09-2021	143	92.2	144	92.9
29-03-2022	121	78	-	-
25-04-2022	141	91	131	84.5
14-05-2022	141	91	147	94.8
24-05-2022	140	90.3	146	94.1
30-06-2022	102	65.8	-	-
30-07-2022	-	-	145	93.5
15-08-2022	-	-	145	93.5
15-09-2022	-	-	144	93
19-03-2023	-	-	138	89
28-04-2023	-	-	143	92.2
25-05-2023	-	-	148	95.5
25-06-2023	-	-	144	92.9
29-07-2023	-	-	140	90.3

669 **Appendix D:** Time lapse inversion results

670 Appendix D presents time- lapse inversions of a large number of datasets from north-west face
671 and south faces. The Resistivity variation ratio between consecutive electrical resistivity
672 tomograms is also evaluated. A summary of these datasets is provided in Table 1C.

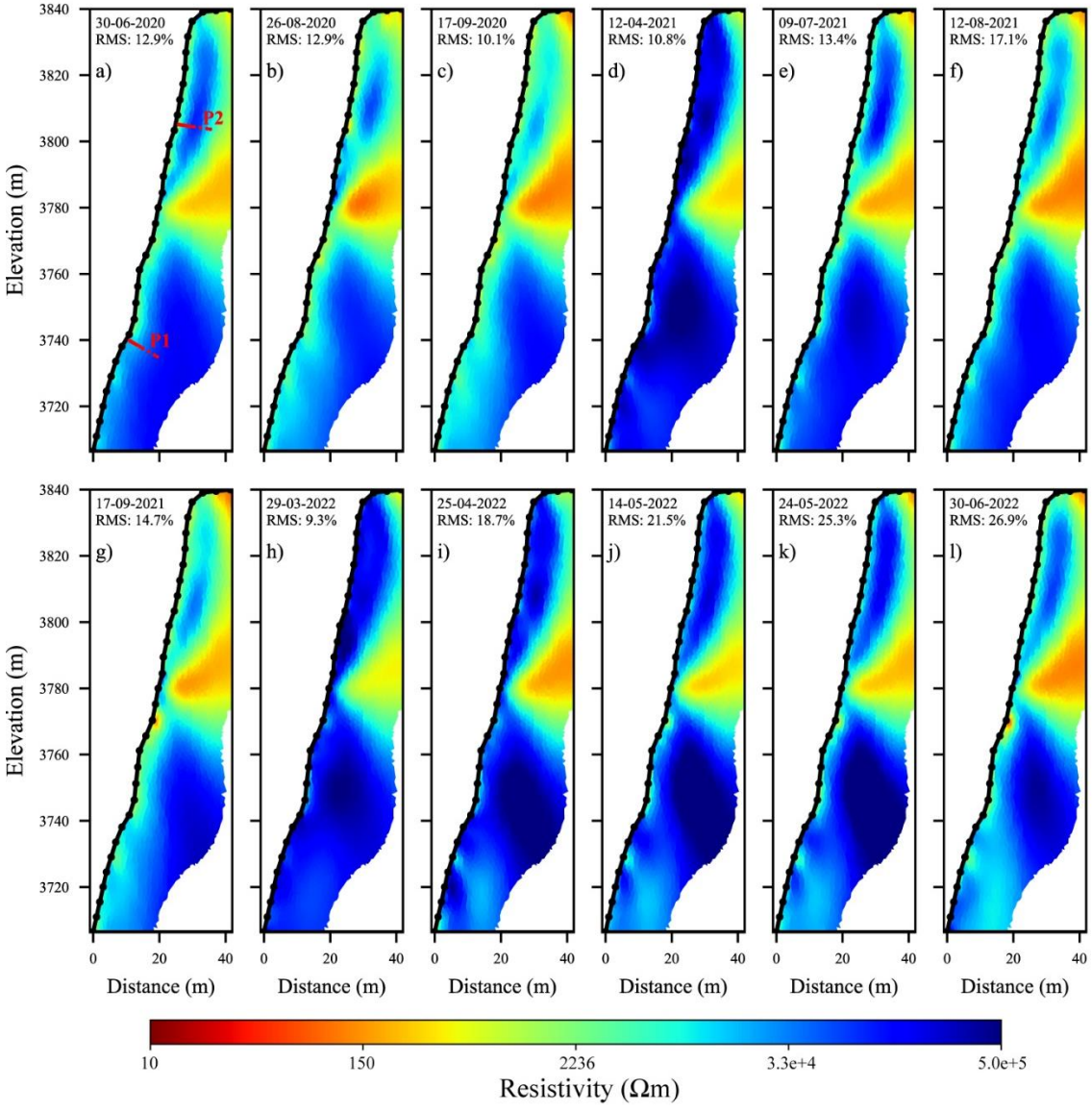

673

674 **Figure D1.** Electrical resistivity tomograms at different dates (from June-2020 to June-2022) along the
675 NW side (NW profile). The conductive zone (in warm colors) indicates the presence of the gallery and
676 elevator (see Fig. 6). The red dots (P1 in panel a) indicate the positions of the thermal sensors in the
677 borehole BH-NW. Data presented on Figures 9, 10 and 11 are extracted at the red dots (P1 and P2).

678

679

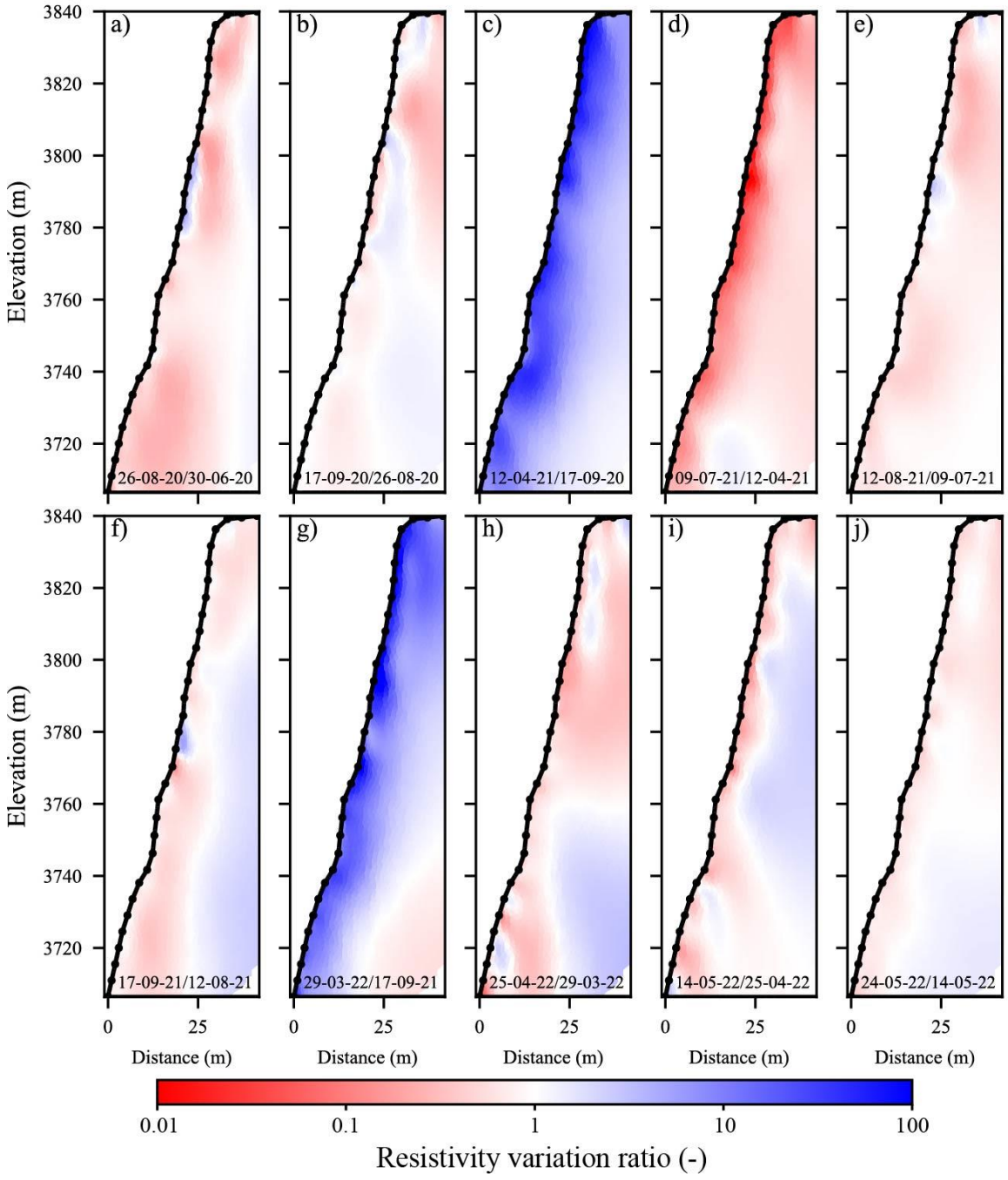

680

681 **Figure D2.** Resistivity variation ratio between consecutive electrical resistivity tomograms (shown in
682 Fig. 9) along the NW side. Blue colors indicate an increase in resistivity, while red colors represent a
683 decrease in resistivity from one measurement to the next.

684

685 Figure C3 illustrates the resistivity variation ratio between successive measurements on
686 the S profile (Figure 12). The dynamics of the active layer are evident, with freezing-thawing
687 effects visible near the surface (*e.g.*, Fig. D3a, d, and g). The heat effect (*i.e.*, decrease in

688 resistivity values near the surface) is more pronounced in the lower section (below the gallery).
689 Another type of anomaly could be observed at greater depth, where heat and/or cool waves
690 resulting of heat transfer (with delay) lead to local variations at greater depth (*e.g.*, Fig. D3, e,
691 g and i). In contrast, the fractured zone in the upper portion obscures the temperature
692 dependency of resistivity due to fluctuations in air and water content (*i.e.*, resistivity in this zone
693 is impacted by factors beyond just temperature). Water infiltration in this area could explain the
694 rapid and significant decrease in resistivity observed between 3790 and 3820 m a.s.l. (*e.g.*, Fig.
695 D3c, f, and j), which increases the thickness of active layer in this zone.

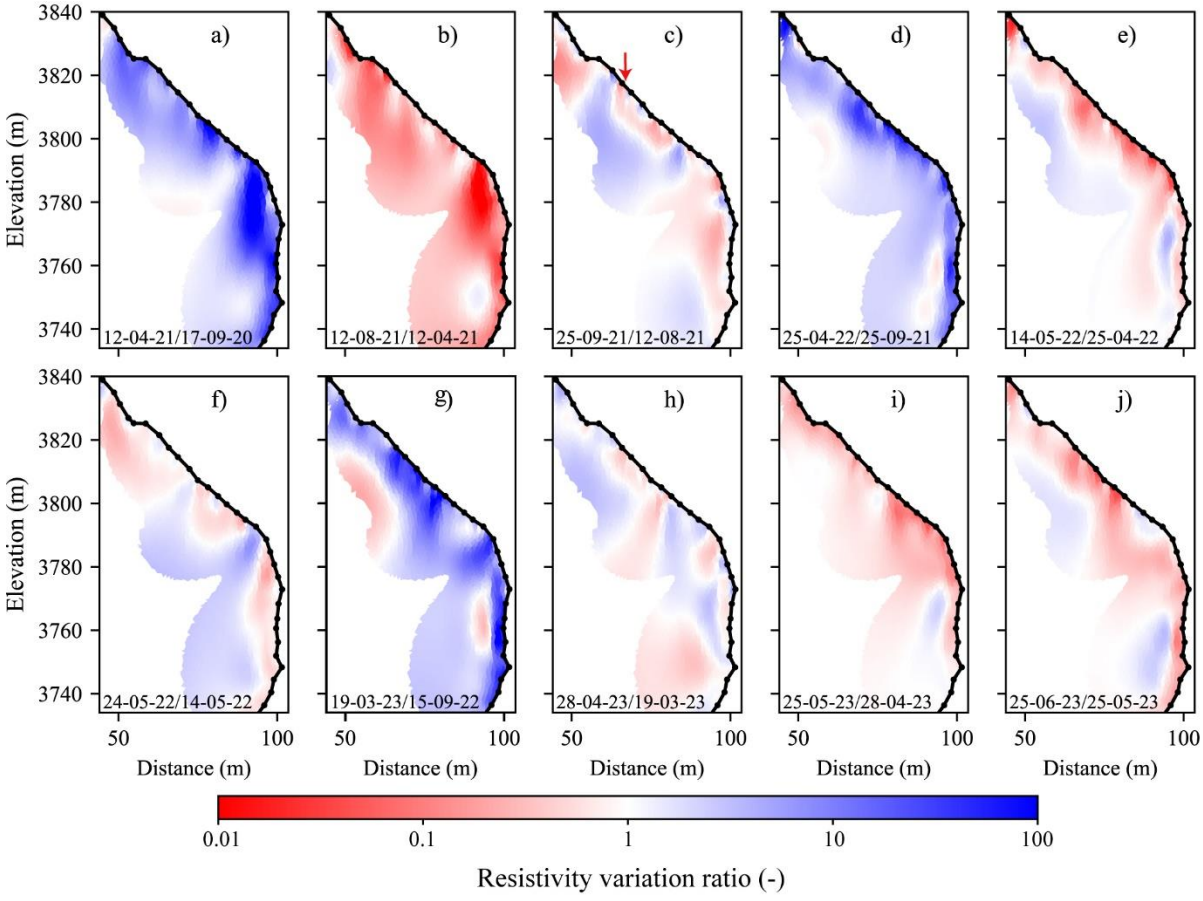

696

697 Figure D3. Resistivity variation ratio between consecutive electrical resistivity tomograms (shown in
698 Fig. 11) along the South side. Blue colors indicate an increase in resistivity, while red colors represent
699 a decrease in resistivity from one measurement to the next. The red arrow shows the position of
700 possible water infiltration.

701

References

Abdulsamad, F., Revil, A., Ghorbani,A., Toy, V., Kirilova, M., Coperey, A., Duvillard, P. A., Ménard, G., and Ravanel, L. Complex conductivity of graphitic schists and sandstones. Journal of Geophysical Research: Solid Earth, 124, 8223‐8249. https://doi.org/10.1029/2019JB017628, 2019.

Ben-Asher, M., Magnin, F., Westermann, S., Bock, J., Malet, E., Berthet, J., Ravanel, L., and Deline, P.: Estimating surface water availability in high mountain rock slopes using a numerical energy balance model, Earth Surf. Dynam., 11, 899–915, https://doi.org/10.5194/esurf-11-899-2023, 2023.

Binley, A. and Kemna, A.: DC Resistivity and Induced Polarization Methods, in: Hydrogeophysics, Water Science and Technology Library book series, edited by: Rubin, Y. and Hubbard, S. S.,volume 50, 129‐156, https://doi.org/10.1007/1-4020-3102-5_5, 2005.

Campbell, S., Rosa T. Affleck, Sinclair, S. Ground-penetrating radar studies of permafrost, periglacial, and near-surface geology at McMurdo Station, Antarctica. Cold Regions Science and Technology, 148, Pages 38-49, https://doi.org/10.1016/j.coldregions.2017.12.008, 2018.

Cathala, M., Bock, J., Abdulsamad, F., Deline, P., Josnin, J-Y., Ravanel, L., Revil, A., Richard, J., Verroust, F., and Magnin, F. Assessing the role of permafrost in the preconditioning and triggering factors of the September 2020 Crête des Grangettes rockfall (southern French Alps), Géomorphologie: relief, processus, environnement, 30, 3, 171-188, https://doi.org/10.4000/12yqn, 2024.

Coperey, A., Revil, A., Abdulsamad, F., Stutz, B., Duvillard, P.A., and Ravanel, L. Low frequency induced polarization of porous media undergoing freezing: preliminary observations and modeling, Journal of Geophysical Research: Solid Earth, 124, doi:10.1029/2018JB017015, 2019.

Dahlin, T., and Zhou, B. A numerical comparison of 2D resistivity imaging with 10 electrode arrays, Geophys. Prospect., 52, 379–398. https://doi.org/10.1111/j.1365-2478.2004.00423.x, 2004.

Doetsch, J., Ingeman-Nielsen, T., Christiansen, A. V., Fiandaca, G., Auken, E., and Elberling, B.: Direct current (DC) resistivity and induced polarization (IP) monitoring of active layer dynamics at high

temporal resolution, Cold Reg. Sci. Technol., 119, 16‑28, https://doi.org/10.1016/j.coldregions.2015.07.002, 2015.

Draebing, D. Application of refraction seismics in alpine permafrost studies: A review, Earth-Science Reviews, 155, 136–152, https://doi.org/10.1016/j.earscirev.2016.02.006, 2016.

Duvillard, P. A., Revil, A., Qi, Y., Soueid Ahmed, A., Coperey, A., and Ravanel, L.: Three-Dimensional Electrical Conductivity and Induced Polarization Tomography of a Rock Glacier, J. Geophys. Res.-Sol. Ea., 123, 9528‑9554, https://doi.org/10.1029/2018JB015965, 2018.

Duvillard, P.A., Magnin, F., Revil, A., Legay, A., Ravanel, L., Abdulsamad, F., and Coperey, A.: Temperature distribution in a permafrost-affected rock ridge from conductivity and induced polarization tomography, Geophys. J. Int., 225, 1207‑1221, https://doi.org/10.1093/gji/ggaa597, 2021.

Edwards, S. L.: A modified pseudosection for resistivity and IP. *Geophysics*, 42, 1020–1036, https://doi.org/10.1190/1.1440762, 1977.

Etzelmüller, B., Czekirda, J., Magnin, F., Duvillard, P.-A., Ravanel, L., Malet, E., Aspaas, A., Kristensen, L., Skrede, I., Majala, G. D., Jacobs, B., Leinauer, J., Hauck, C., Hilbich, C., Böhme, M., Hermanns, R., Eriksen, H. Ø., Lauknes, T. R., Krautblatter, M., and Westermann, S.: Permafrost in monitored unstable rock slopes in Norway – new insights from temperature and surface velocity measurements, geophysical surveying, and ground temperature modelling, Earth Surf. Dynam., 10, 97–129, https://doi.org/10.5194/esurf-10-97-2022, 2022.

Farzamian M, Vieira G, Monteiro Santos FA, et al. Detailed detection of active layer freeze-thaw dynamics using quasi-continuous electrical resistivity tomography (Deception Island, Antarctica). Cryosphere.14(3):1105-1120. https://doi.org/10.5194/tc-14-1105-2020, 2020.

Günther, T., Rücker, C., and Spitzer, K. Three-dimensional modelling and inversion of dc resistivity data incorporating topography-II. Inversion. Geophysical Journal International, Volume 166, Issue 2, August 2006, Pages 506–517, https://doi.org/10.1111/j.1365-246X.2006.03011.x, 2006.

Hartmeyer, I., Delleske, R., Keuschnig, M., Krautblatter, M., Lang, A., Schrott, L., and Otto, J.-C.: Current glacier recession causes significant rockfall increase: the immediate paraglacial response

of deglaciating cirque walls, Earth Surf. Dynam., 8, 729–751, https://doi.org/10.5194/esurf-8-729-2020, 2020.

Hasler, A., Gruber. S., Font. M., and Dubois. A. Advective Heat Transport in Frozen Rock Clefts: Conceptual Model, Laboratory Experiments and Numerical Simulation, Permafrost and Periglacial Processes, 22, 378–389, https://doi.org/10.1002/ppp.737, 2011.

Hauck, C., Böttcher, M., and Maurer, H.: A new model for estimating subsurface ice content based on combined electrical and seismic data sets, The Cryosphere, 5, 453–468, https://doi.org/10.5194/tc-5-453-2011, 2011.

Hauck, C., and Hilbich C. Preconditioning of mountain permafrost towards degradation detected by electrical resistivity. Environ. Res. Lett. 19 064010. https://doi.org/10.1088/1748-9326/ad3c55, 2024.

Herring, T., Lewkowicz, A. G., Hauck, C., Hilbich, C., Mollaret, C., Oldenborger, G. A., Uhlemann, S., Farzamian, M., Calmels, F., and Scandroglio, R.: Best practices for using electrical resistivity tomography to investigate permafrost, Permafrost Periglac., 34, 494–512, https://doi.org/10.1002/ppp.2207, 2023.

Hilbich, C., Marescot, L., Hauck, C., Loke, M. H., and Mäusbacher, R.: Applicability of Electrical Resistivity Tomography Monitoring to Coarse Blocky and Ice-rich Permafrost Landforms, Permafrost Periglac., 20, 269–284, https://doi.org/10.1002/ppp.652, 2009.

Hilbich, C., Hauck, C., Hoelzle, M., Scherler, M., Schudel, L., Völksch, I., Vonder Mühll, D., and Mäusbacher, R. Monitoring Mountain permafrost evolution using electrical resistivity tomography: A 7-year study of seasonal, annual, and long-term variations at Schilthorn, Swiss Alps, J. Geophys. Res.-Earth, 113, F01S90, https://doi.org/10.1029/2007JF000799, 2008.

Jacquemart, M., Weber, S., Chiarle, M., Chmiel, M., Cicoira, A., Corona, C., Eckert, N., Gaume, J., Giacona, F., Hirschberg, J., Kaitna, R., Magnin, F., Mayer, S., Moos, C., van Herwijnen, A., and Stoffel, M.: Detecting the impact of climate change on alpine mass movements in observational records from the European Alps, Earth-Science Reviews, 258, 104886, https://doi.org/10.1016/j.earscirev.2024.104886, 2024.

Karaoulis, M., Tsourlos, P., Kim, J., and Revil, A.: 4D time-lapse ERT inversion: introducing combined time and space constraints, Near Surf. Geophys., 12, 25–34, https://doi.org/10.3997/1873-0604.2013004, 2013.

Keuschnig, M., Krautblatter,M., Hartmeyer, I., Fuss, C. and Schrott, L.: Automated electrical resistivity tomography testing for early warning in unstable permafrost rock walls around Alpine infrastructure, Permafrost Periglac., 28, 158–171. https://doi.org/10.1002/ppp.1916, 2017.Krautblatter, M. and Hauck, C.: Electrical resistivity tomography monitoring of permafrost in solid rock walls, J. Geophys. Res., 112, F02S20, https://doi.org/10.1029/2006JF000546, 2007.

Krautblatter M, Verleysdonk S, Flores-Orozco A., and Kemna A.: Temperature-calibrated imaging of seasonal changes in permafrost rock walls by quantitative electrical resistivity tomography (Zugspitze, German/Austrian Alps). J. Geophys. Res., 115, F02003, https://doi.org/10.1029/2008JF001209, 2010.

Krautblatter, M., Funk, D. and G¨unzel, F.K. Why permafrost rocks become unstable: a rock–ice-mechanical model in time and space. Earth Surf. Process. Landforms, 38, 876–887. https://doi.org/10.1002/esp.3374, 2013.

Loke, M. H. Time-lapse resistivity imaging inversion, paper presented at 5th Meeting of the Environmental and Engineering Society European Section, Budapest. 1999.

Magnin, F., Deline, P., Ravanel, L., Noetzli, J., and Pogliotti, P.: Thermal characteristics of permafrost in the steep alpine rock walls of the Aiguille du Midi (Mont Blanc Massif, 3842 m a.s.l), The Cryosphere, 9, 109–121, https://doi.org/10.5194/tc-9-109-2015, 2015b.

Magnin, F., Krautblatter, M., Deline, P., Ravanel, L., Malet, E. and Bevington, A.: Determination of warm, sensitive permafrost areas in near-vertical rockwalls and evaluation of distributed models by electrical resistivity tomography, J. geophys. Res.-Earth, 120, 745–762, https://doi.org/10.1002/2014JF003351, 2015a.

Magnin, F., Ravanel, L., Bodin, X., Deline, P., Malet, E., Krysiecki, J.-M., et al. Main results of permafrost monitoring in the French Alps through the PermaFrance network over the period 2010–2022. Permafrost and Periglacial Processes, 35(1), 3–23. https://doi.org/10.1002/ppp.2209, 2024

Magnin, F. and Josnin, J.-Y. Water flows in Rock Wall permafrost: a numerical approach coupling hydrological and thermal processes. Journal of Geophysical Research - Earth Surface, 126(11), e2021JF006394. https://doi.org/10.1029/2021JF006394, 2021.

Magnin, F., Josnin, J.-Y., Ravanel, L., Pergaud, J., Pohl, B., and Deline, P.: Modelling rock wall permafrost degradation in the Mont Blanc massif from the LIA to the end of the 21st century, The Cryosphere, 11, 1813–1834, https://doi.org/10.5194/tc-11-1813-2017, 2017.

Maierhofer, T., Flores Orozco, A., Roser, N., Limbrock, J. K., Hilbich, C., Moser, C., Kemna, A., Drigo, E., Morra di Cella, U., and Hauck, C.: Spectral induced polarization imaging to monitor seasonal and annual dynamics of frozen ground at a mountain permafrost site in the Italian Alps, The Cryosphere, 18, 3383–3414, https://doi.org/10.5194/tc-18-3383-2024, 2024.

Mewes, B., Hilbich, C., Delaloye, R., and Hauck, C.: Resolution capacity of geophysical monitoring regarding permafrost degradation induced by hydrological processes, The Cryosphere, 11, 2957–2974, https://doi.org/10.5194/tc-11-2957-2017, 2017.

Mollaret, C., Wagner, F. M., Hilbich, C., Scapozza, C., and Hauck, C.: Petrophysical Joint Inversion Applied to Alpine Permafrost Field Sites to Image Subsurface Ice, Water, Air, and Rock Contents, Front. Earth Sci., 8, 1–25, https://doi.org/10.3389/feart.2020.00085, 2020.

Mollaret, C., Hilbich, C., Pellet, C., Flores-Orozco, A., Delaloye, R., and Hauck, C.: Mountain permafrost degradation documented through a network of permanent electrical resistivity tomography sites, The Cryosphere, 13, 2557–2578, https://doi.org/10.5194/tc-13-2557-2019, 2019.

Noetzli J., Gruber S., Kohl T., Salzmann N., Haeberli W. Three-dimensional distribution and evolution of permafrost temperatures in idealized high-mountain topography. Journal of Geophysical Research: Earth Surface 112, n/a–n/a. https://doi.org/10.1029/2006JF000545, 2007.

Noetzli, J., Isaksen, K., Barnett, J. et al. Enhanced warming of European mountain permafrost in the early 21st century. Nat Commun 15, 10508 (2024). https://doi.org/10.1038/s41467-024-54831-9.

Moser, C., Morra di Cella, U., Hauck, C., and Flores Orozco, A.: Spectral induced polarization survey for the estimation of hydrogeological parameters in an active rock glacier, The Cryosphere, 19, 143–171, https://doi.org/10.5194/tc-19-143-2025, 2025.

836 Offer, M., Weber, S., Krautblatter, M., Hartmeyer, I., and Keuschnig, M.: Pressurised water flow in
837 fractured permafrost rocks revealed by borehole temperature, electrical resistivity tomography, and
838 piezometric pressure, The Cryosphere, 19, 485–506, https://doi.org/10.5194/tc-19-485-2025, 2025.
839 Pavoni, M., Boaga, J., Wagner, F. M., Bast, A., Phillips, M. Characterization of rock glaciers
840 environments combining structurally-coupled and petrophysically-coupled joint inversions of
841 electrical resistivity and seismic refraction datasets, Journal of Applied Geophysics, 215, 0926-
842 9851, https://doi.org/10.1016/j.jappgeo.2023.105097, 2023.
843 Piolat, L., Revil, A., Richard, J., Ghorbani G., Cosme, P., Géraud, Y., Casotti, C., Vaudelet, P., Diraison,
844 M., and Favier, A., 2025.Induced polarization of volcanic rocks. 8. The case of intrusive igneous
845 rocks. Submitted, Geophysical Journal International
846 Ravanel, L., Magnin, F. and Deline, P. Impacts of the 2003 and 2015 summer heatwaves on permafrost-
847 affected rock-walls in the Mont Blanc massif. Science of the Total Environment, 609, 132–143.
848 https://doi.org/10.1016/j.scitotenv.2017.07.055, 2017.
849 Revil, A., Cathles, L. M., Losh, S., & Nunn, J. A. Electrical conductivity in shaly sands with geophysical
850 applications. Journal of Geophysical Research, 103(B10), 23,925–23,936.
851 https://doi.org/10.1029/98JB02125, 1998.
852 Revil, A., Ghorbani, A., Zhao, X., Mouyeaux, A., Barrère, L., Richard, J., Peyras, L., and Vaudelet, P.
853 Groundwater flow paths using combined self-potential, electrical resistivity, and induced
854 polarization signals, Geophysical Journal International, 239, 2, 798–
855 820, https://doi.org/10.1093/gji/ggae291, 2024.
856 Revil, A., Coperey, A., Mao, D., Abdulsamad, F., Ghorbani, A., Rossi, M., and Gasquet, D,. Induced
857 polarization response of porous media with metallic particles — Part 8: Influence of temperature
858 and salinity: Geophysics, 83, no. 6, E435–E456, https://doi.org/10.1190/geo2018-0089.1, 2018.
859 Rücker, C., Günther, T., and Wagner, F. M.: pyGIMLi: An open-source library for modelling and
860 inversion in geophysics, Computers & Geosciences, 109, 106–123,
861 https://doi.org/10.1016/j.cageo.2017.07.011, 2017.

862 Scandroglio, R., Draebing, D., Offer, M., Krautblatter, M.: 4D quantification of alpine permafrost
863 degradation in steep rock walls using a laboratory-calibrated electrical resistivity tomography
864 approach, Near Surface Geophys., 19, 241-260, https://doi.org/10.1002/nsg.12149, 2021.
865 Smith, S.L., O'Neill, H.B., Isaksen, K. et al. The changing thermal state of permafrost. Nat Rev Earth
866 Environ 3, 10–23 (2022). https://doi.org/10.1038/s43017-021-00240-1
867 Steiner, M., Wagner, F. M., and Flores Orozco, A.: Improved characterization of alpine permafrost
868 through structurally constrained inversion of refraction seismic data, The Cryosphere Discuss,
869 https://doi.org/10.5194/tc-2019-52, 2019.
870 Steiner, M., Wagner, F. M., Maierhofer, T., Schöner, W., and Flores Orozco, A. Improved estimation
871 of ice and water contents in alpine permafrost through constrained petrophysical joint inversion:
872 The Hoher Sonnblick case study," GEOPHYSICS 86: WB61-WB75.
873 https://doi.org/10.1190/geo2020-0592.1, 2021.
874 Wagner, F. M., Mollaret, C., Kemna, A., and Hauck, C.: Quantitative imaging of water, ice and air in
875 permafrost systems through petrophysical joint inversion of seismic refraction and electrical
876 resistivity data, Geophys. J. Int., 219, 1866–1875, https://doi.org/10.1093/gji/ggz402, 2019.
877 Zimmermann, E., Kemna, A., Berwix, J., Glaas, W., Münch, H. M., and Huisman, J. A. A high accuracy
878 impedance spectrometer for measuring sediments with low polarizability. Measurement Science
879 and Technology, 19(10), 105603. https://doi.org/10.1088/0957-0233/19/10/105603, 2008.